

SCIENCES

Energy, Field Directors – Alain Dollet and Pascal Brault

Renewable Energies, Subject Head – Abdelilah Slaoui

Concentrating Solar Thermal Energy

Fundamentals and Applications

Coordinated by
Gilles Flamant

Color Section

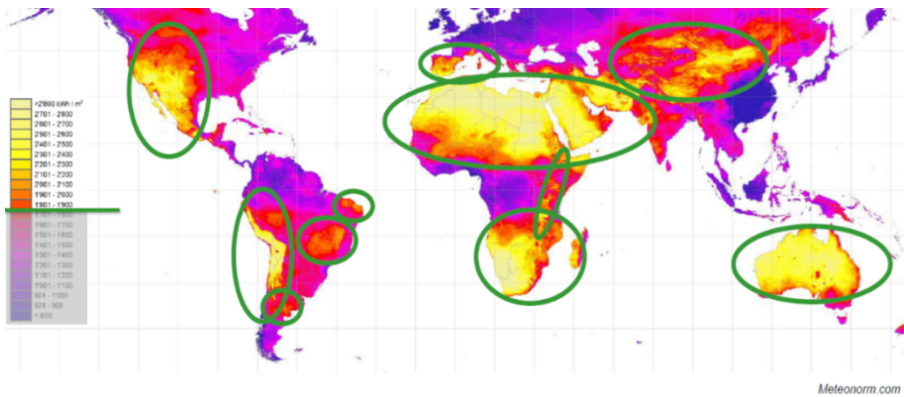


Figure 1.1. Suitable geographical areas for concentrated solar power plant deployment (<https://meteonorm.com/en/>)



Figure 1.2. Solar field of heat generation in Brønderslev (Denmark)



Figure 1.3. *Thémis, operating solar power plant (Targassonne, 66)*



Figure 1.4. *Solar furnace of CNRS at Odeillo-Font-Romeu. In the foreground, the dish–Stirling module being tested*

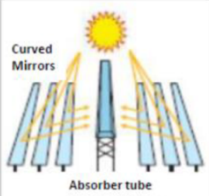
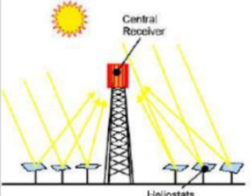
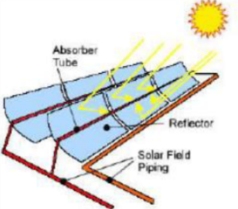
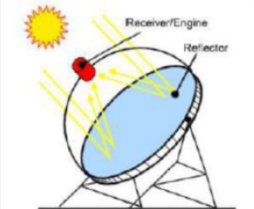
Concentrator/ Receiver	Linear (C = 30-100)	Point (C = 500-10,000)
Fixed	<p>Linear Fresnel system</p> 	<p>Solar power tower</p> 
Mobile	<p>Parabolic trough</p> 	<p>Parabolic</p> 

Figure 1.5. Classification of solar power plants (Solar PACES 2020)

Concentrator/ Receiver	Linear (C = 30-100) 300°C-500°C	Point (C = 500-10,000) 500°C-1500°C
Fixed		
Mobile		

Figure 1.6. Examples of various solar concentrators

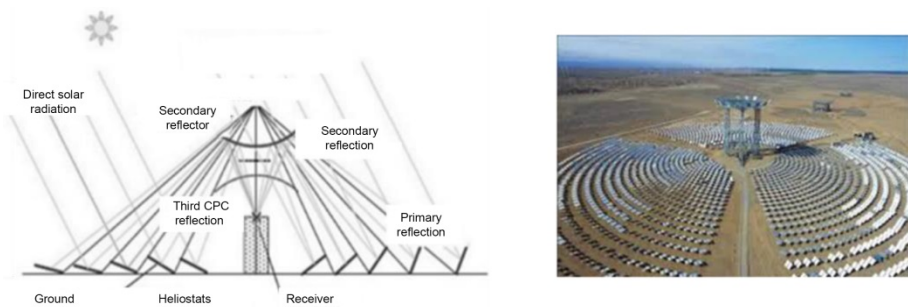


Figure 1.7. On the left, the beam-down concentration optics principle adapted from Gordon and Feuermann 2019 and on the right the 17 MW_{th} Yumen Xinneng industrial installation (China)

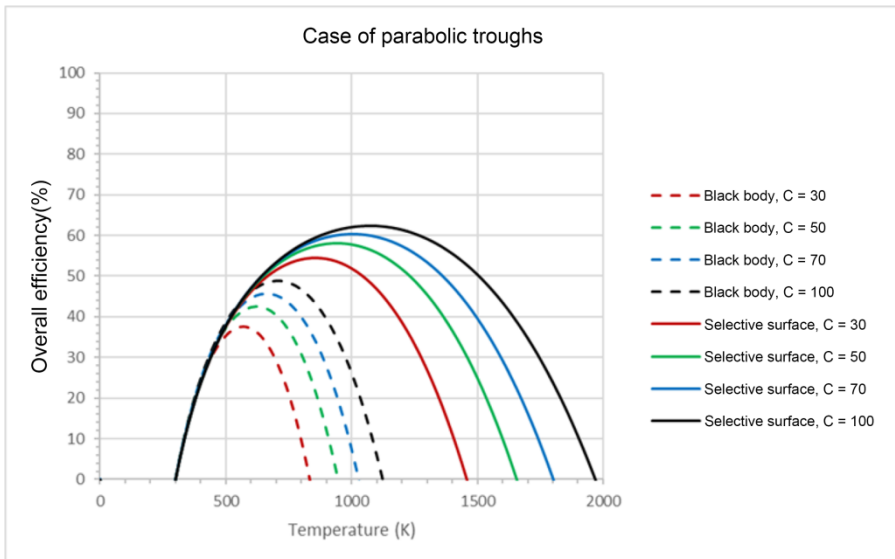


Figure 1.8. Heat to electric power conversion efficiency for linear concentrators, selective surface: $\alpha = 0.95$ and $\epsilon = 0.1$; $I = 900 \text{ W/m}^2$

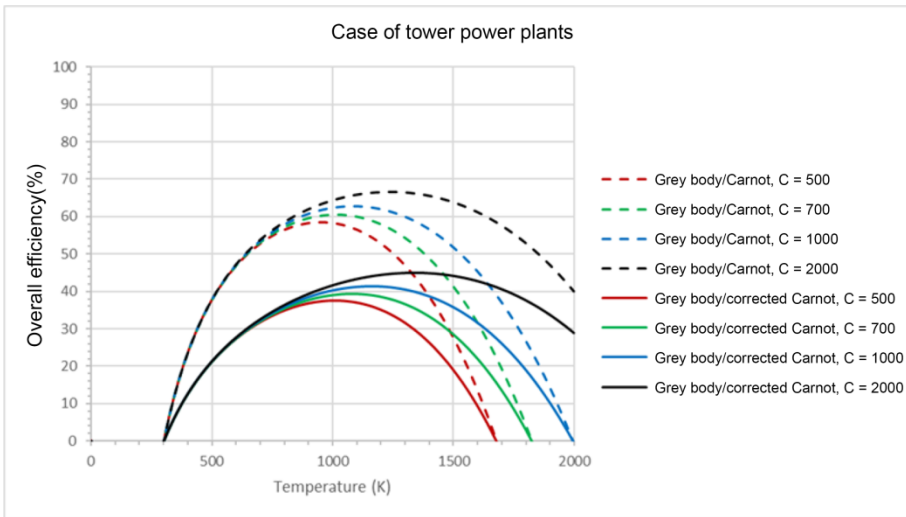


Figure 1.9. Solar heat to electric power conversion efficiency for point concentrators, comparison of conversion efficiency for two hypotheses of converter efficiency formulation, gray body: $\alpha = \epsilon = 0.9$; $I = 900 \text{ W/m}^2$

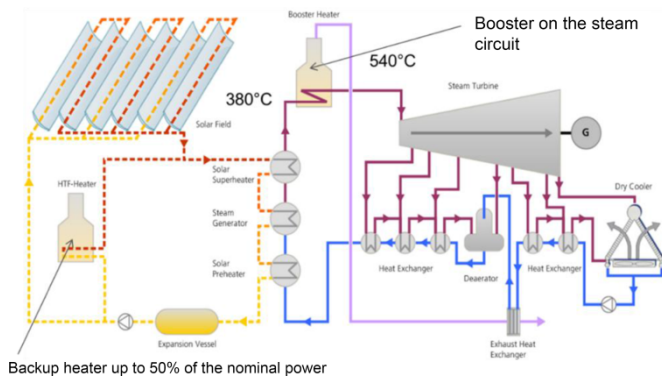


Figure 1.11. Double hybridization architecture of SHAM 1 power plant

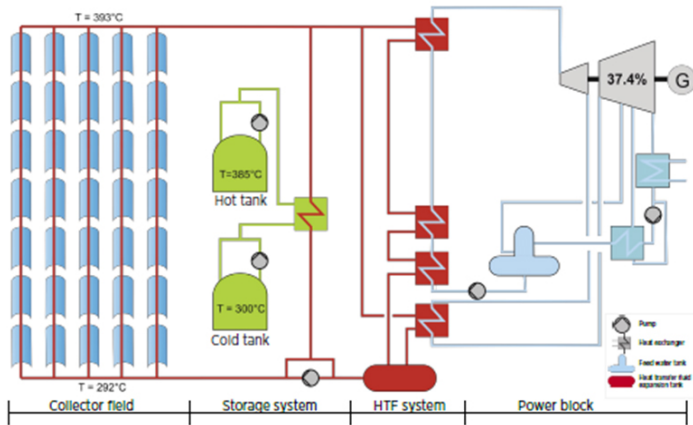


Figure 1.12. The various sub-systems of a parabolic trough solar power plant with molten salt storage. Source DLR



Figure 1.13. Solar power plants ANDASOL 1.2 and 3 of 50 MWe (Spain)



Figure 1.14. A part of the hydraulic circuit of NOOR 1 power plant (Morocco)

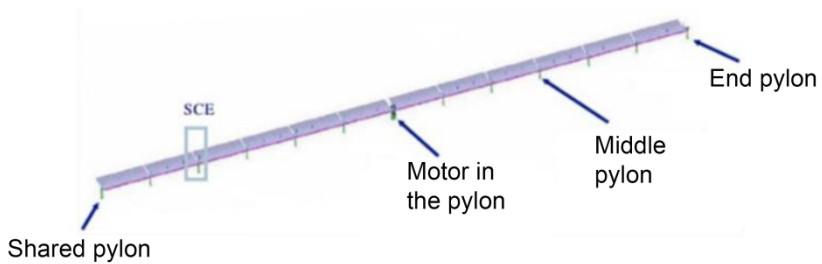


Figure 1.15. Example of solar collector assembly (SCA) in the parabolic trough solar power plant

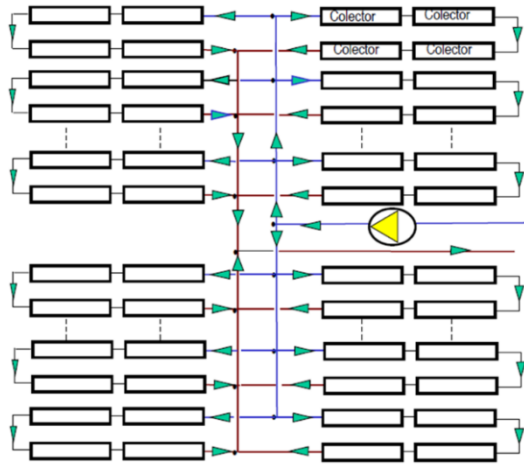


Figure 1.16. *I-shaped architecture of the hydraulic circuit of a PT solar power plant*



Figure 1.17. *Mobile connections at the end of stacks of collectors (NOOR 1 power plant, Morocco)*

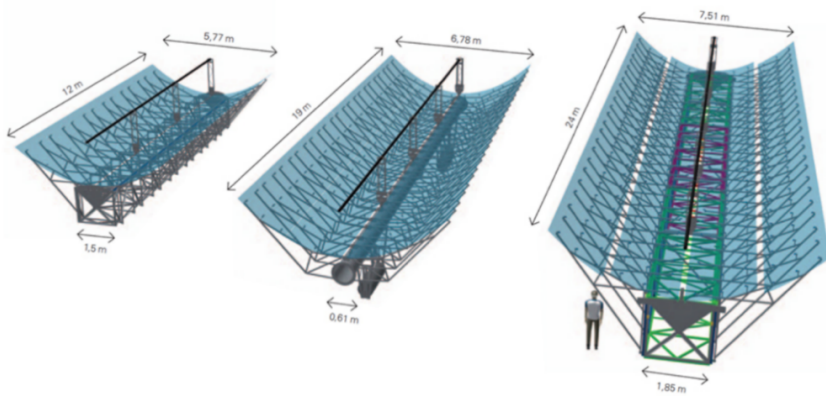


Figure 1.18. Evolution of the size of parabolic-trough concentrators

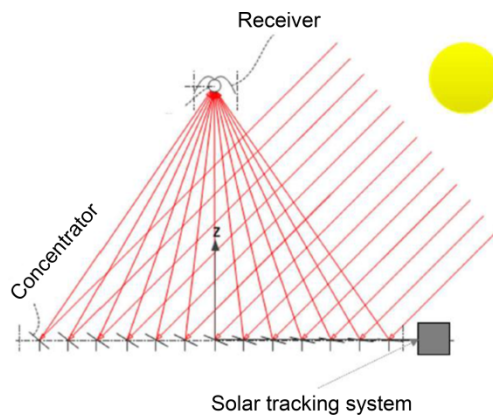


Figure 1.19. Principle of linear Fresnel concentrators (Ko 2019)

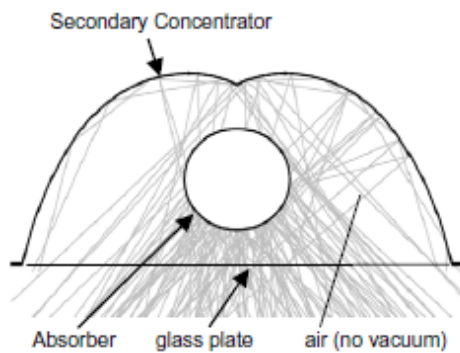


Figure 1.20. Cross-section of a receiver for an LFC solar power plant, example (Morin et al. 2012)



Figure 1.22. *Ivanpah solar power plant, three 130 MW_e towers*
(source: BrightSource Energy)



Figure 1.23. *Gemasolar solar power plant, Spain, source SENER*
(Sener 2020)

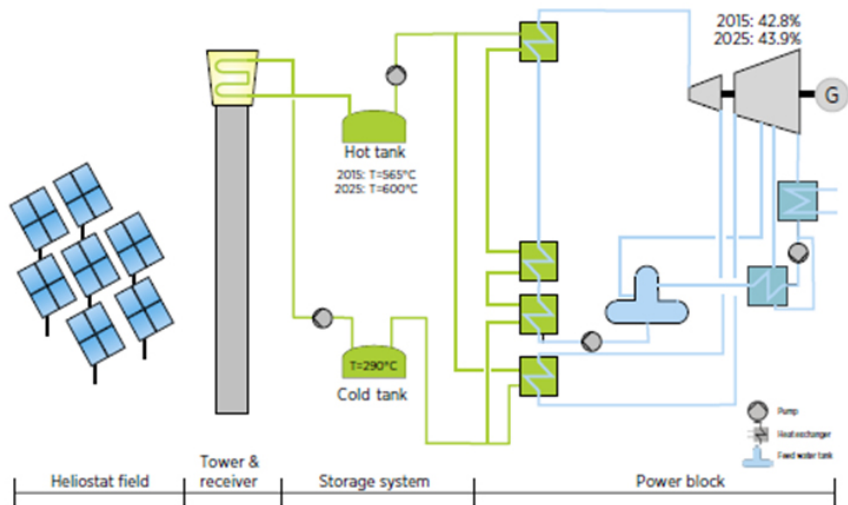


Figure 1.24. Architecture of tower power plants with molten salt. Source: DLR



Figure 1.25. 50 MWe solar power plant in Delingha (China). Source: HELIOSCSP/Supcon

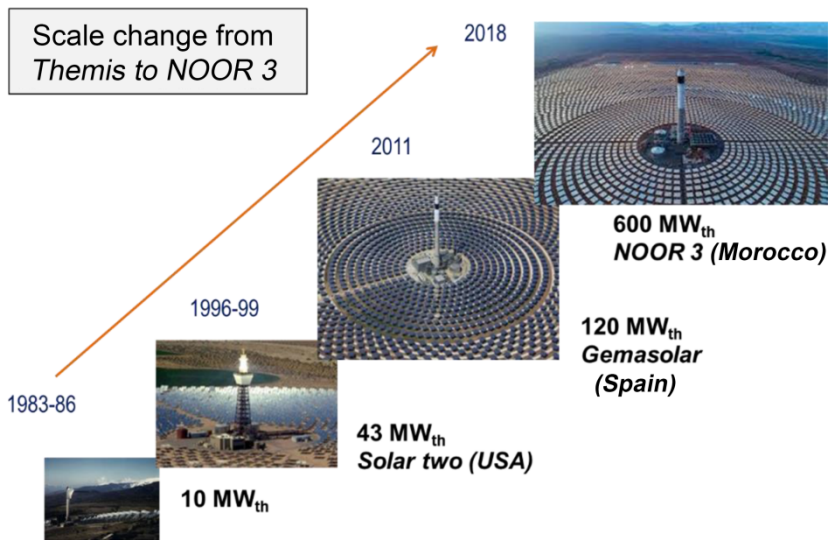


Figure 1.26. Evolution of the thermal power of the solar receiver from Thémis to NOOR 3

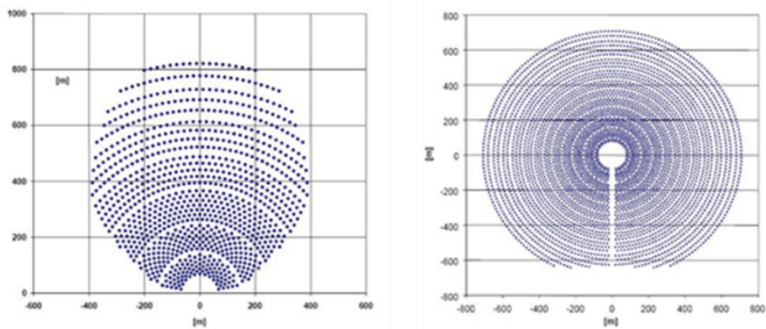


Figure 1.27. Configuration of the heliostat fields of solar tower power plants



Figure 1.28. Heliostat field of 15 m², 47.5 m² and 178 m² (from left to right)

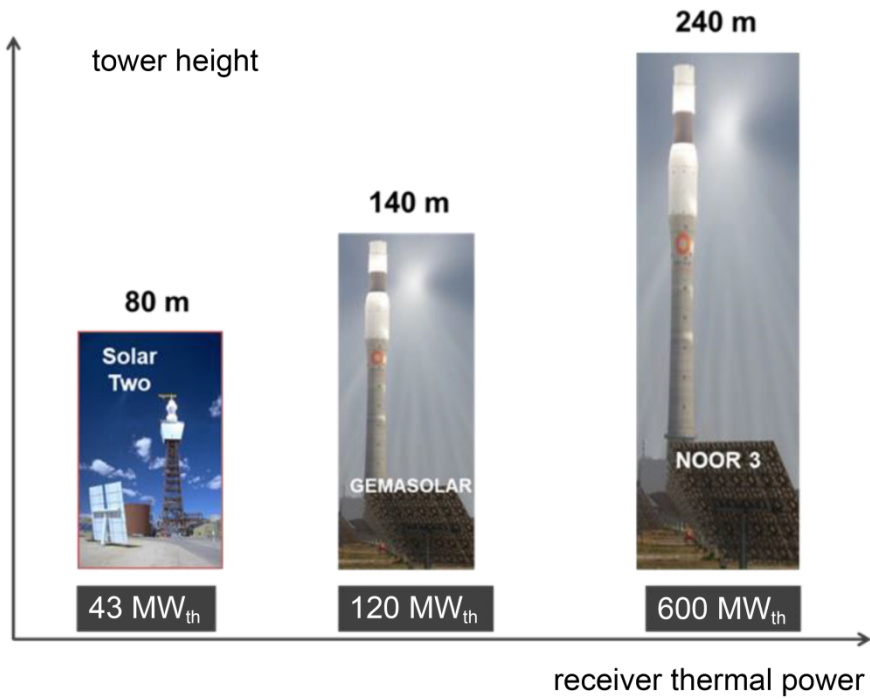


Figure 1.29. Evolution of the height of solar power plant with the power of the receiver



Figure 1.30. On the left, the (25 kWe) Suncatcher, on the right, the (10 kWe) Eurodish module installed at PROMES, Font-Romeu

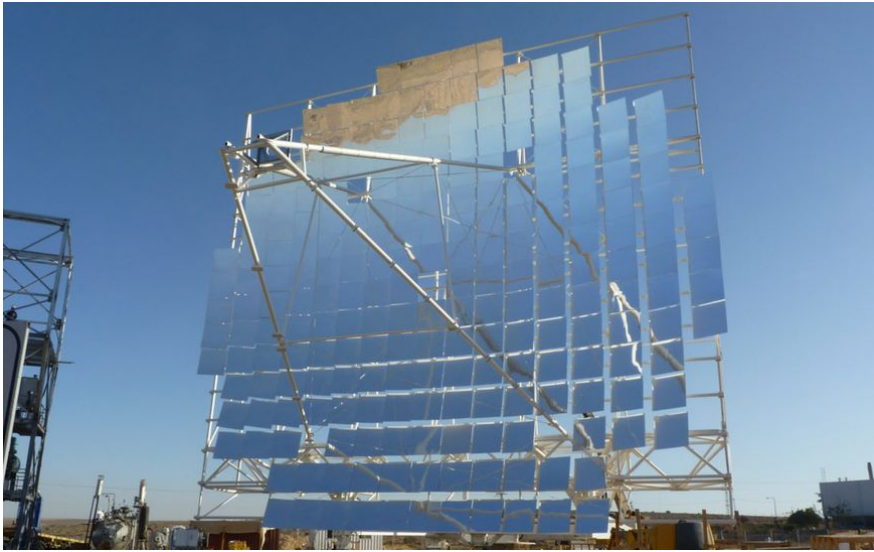


Figure 1.31. HeliFocus parabolic concentrator of 500 m². Source SBP

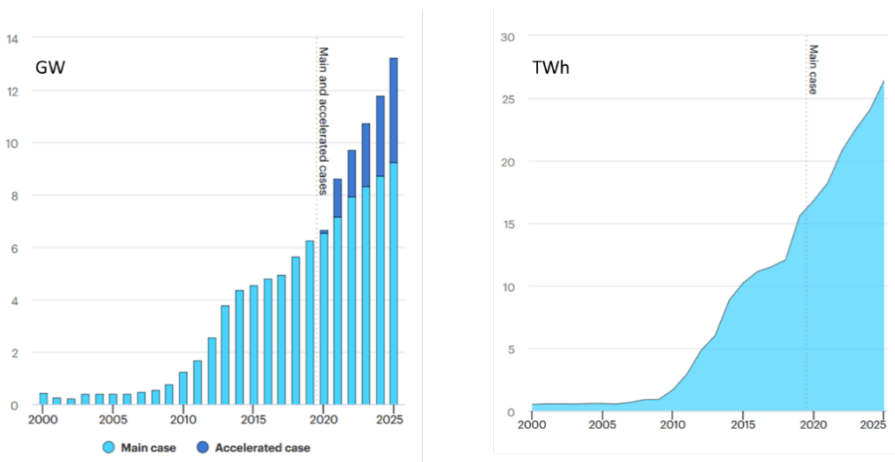


Figure 1.32. Evolution of the installed power and of electricity generation of solar thermal power plants (IEA 2020a)

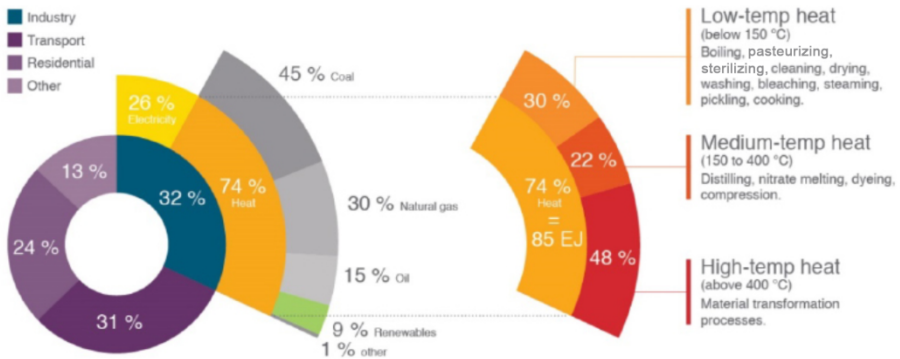


Figure 1.33. Energy consumption of the industry (360 EJ en 2014, 1 EJ = 1018 Joule) and part of the heat at various temperature levels in this consumption (IEA 2020b)

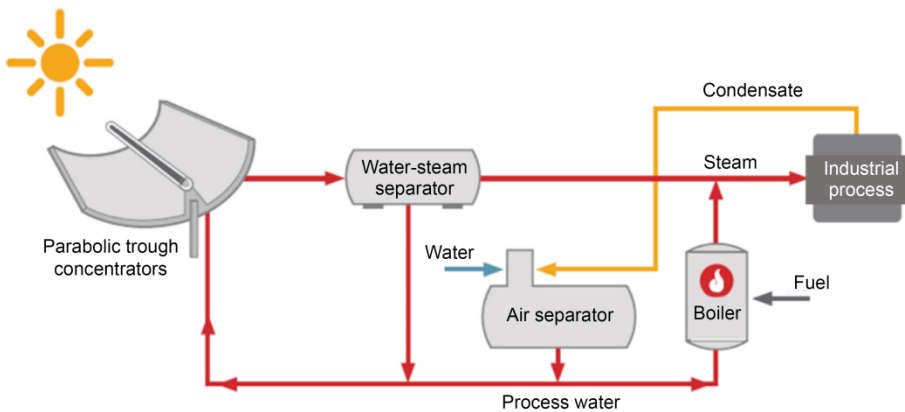


Figure 1.34. Block diagram of a solar installation for steam generation. Parabolic trough concentrators can be replaced by linear Fresnel concentrators



Figure 1.35. Capacity factor of operating solar power plants depending on their storage capacity. Source: IRENA Renewable cost database (IRENA 2019)

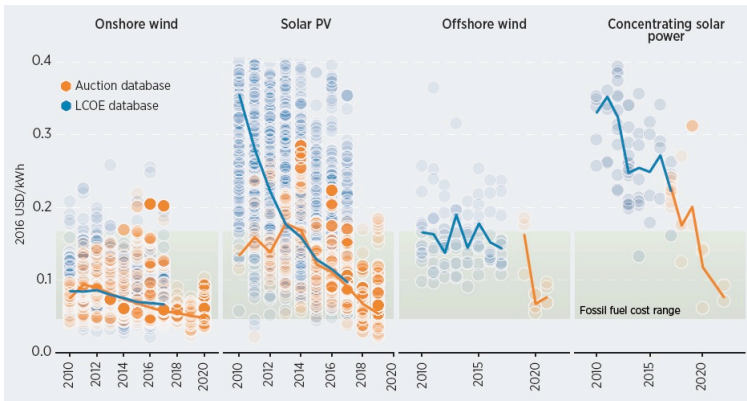


Figure 1.36. Evolution of the levelized cost of electricity and medium value for onshore wind, photovoltaic, offshore wind and concentrated solar power. Each point corresponds to a project. Source: IRENA Renewable cost database and auction database (Irena 2019)

SunShot CSP Progress and Goals



Figure 1.37. Evolution of the levelized cost of solar electricity generated by thermal power plants in the United States and national goals for 2030 (Murphy et al. 2019)

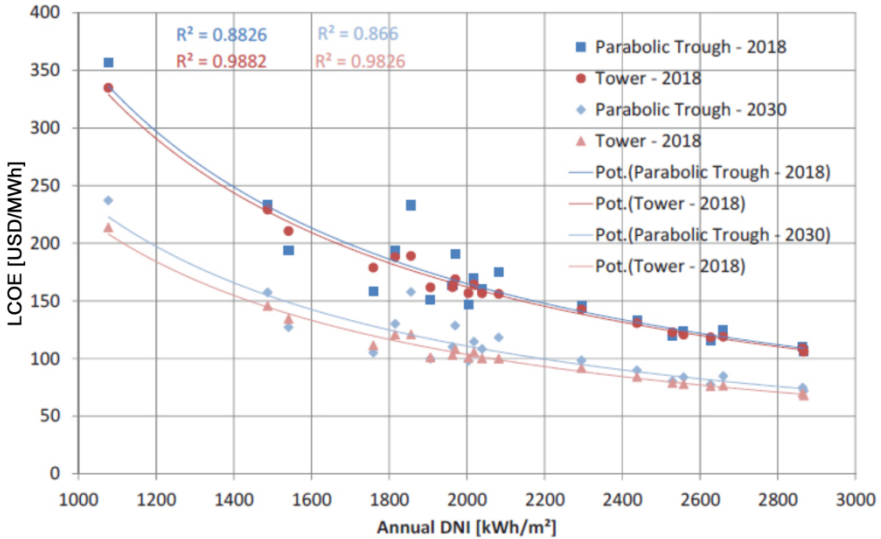


Figure 1.38. Evolution of LCOE depending on DNI in 2018 and 2030 (Dersch et al. 2020). The points correspond to the results of calculations for various sites

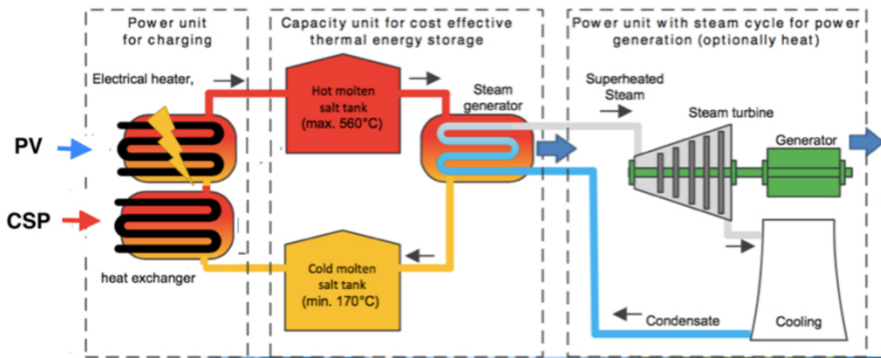


Figure 1.39. Architecture of NOOR Midelt CSP-PV hybrid power plant, Morocco (HELIOSCSP 2020)



Figure 1.40. Jemalong CSP Pilot Plant, pilot solar power plant using sodium as heat transfer fluid (Vast Solar 2020)

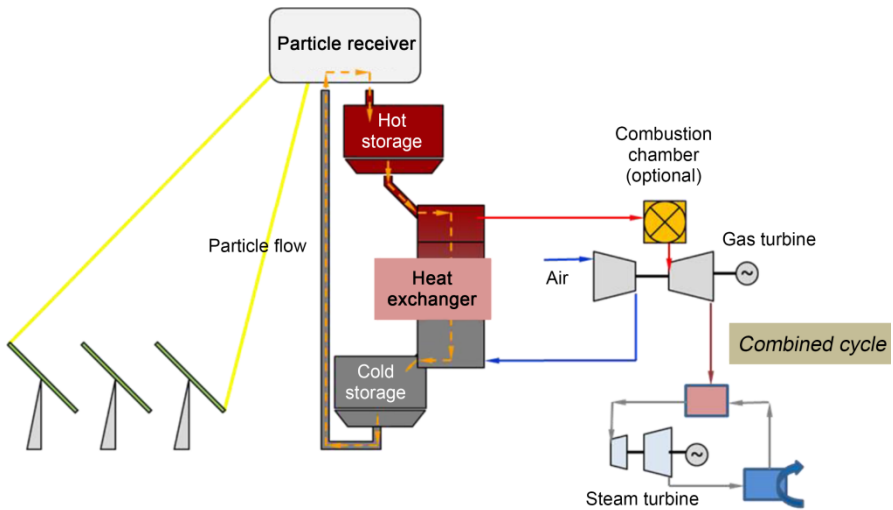


Figure 1.41. Block diagram of a solar power plant with solid heat transfer medium associated with a combined cycle

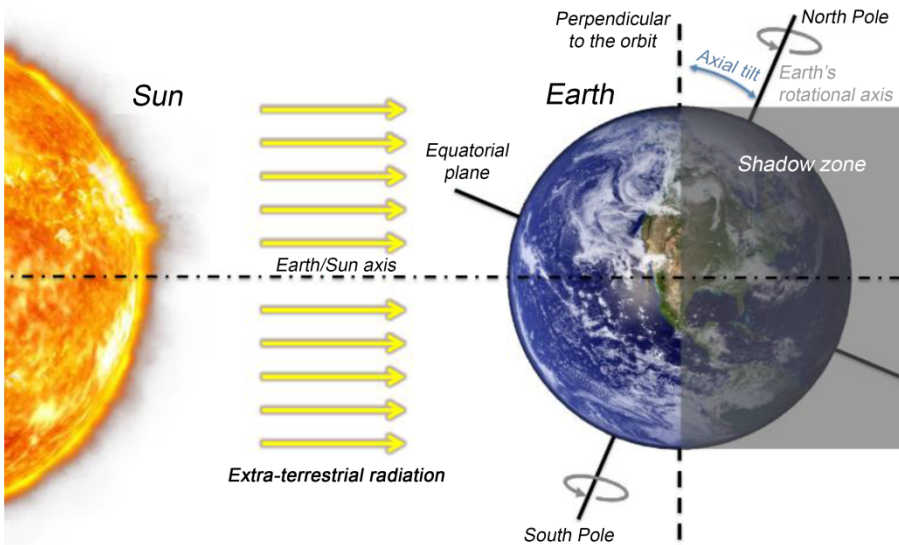


Figure 2.1. Simplified view of the Earth/Sun system

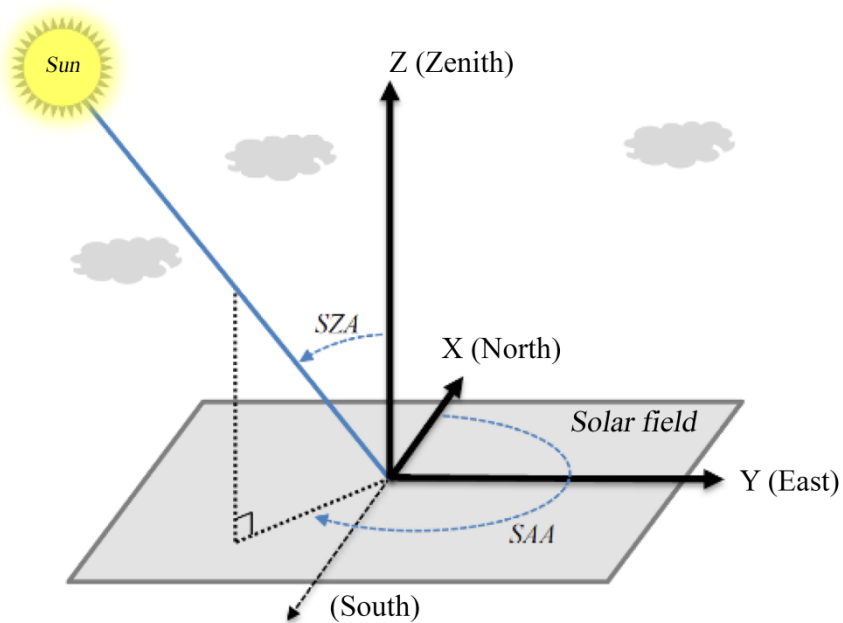


Figure 2.2. Solar/zenith angle (SZA) and solar/azimuth angle (SAA)

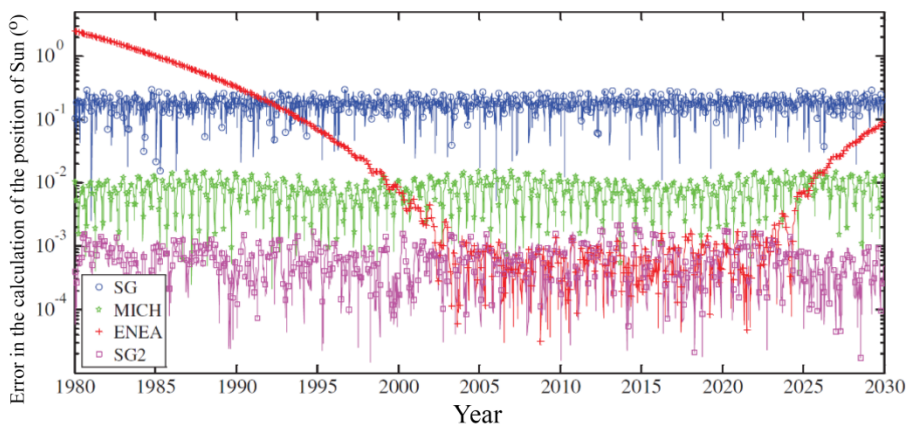


Figure 2.3. Error in the calculation of the position of the Sun, with respect to SPA, for SG, MICH, ENEA and SG2 algorithms, throughout 1980–2030 (Blanc and Wald 2012)

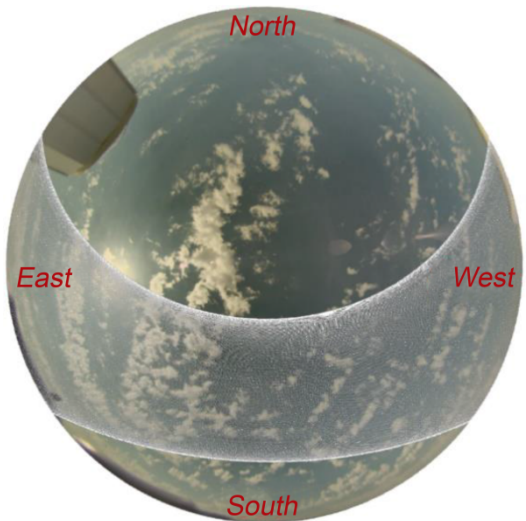


Figure 2.4. Sun's path in 2015 above the PROMES-CNRS laboratory, calculated using the SG2 algorithm

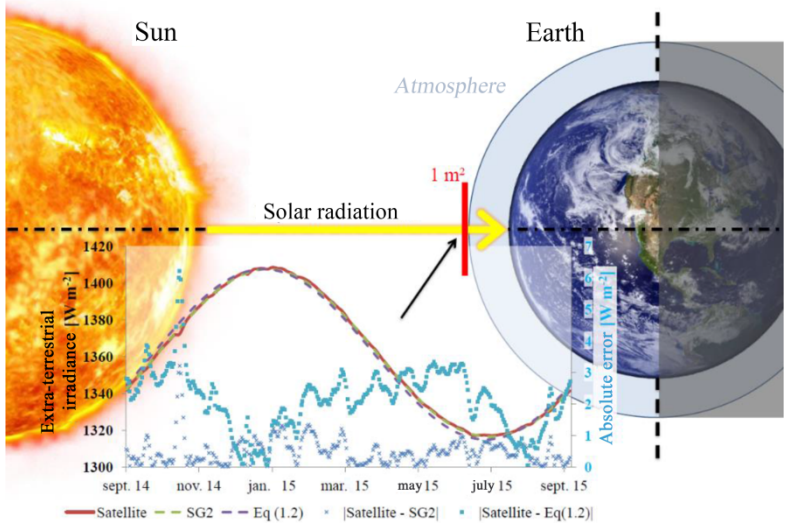


Figure 2.5. Annual variation of the extra-terrestrial irradiance

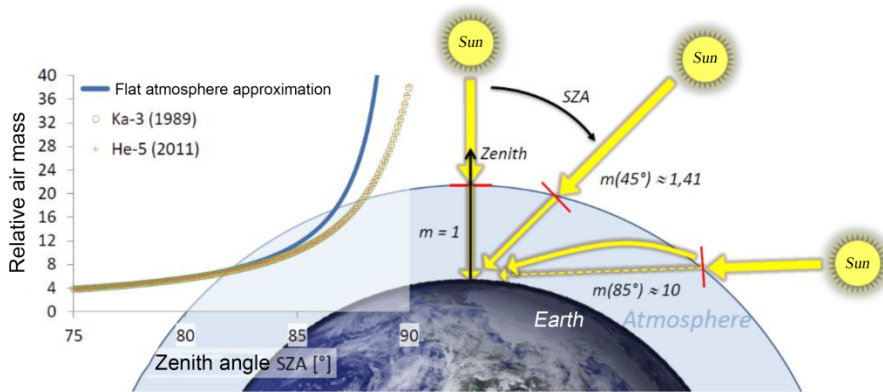


Figure 2.6. Schematic representation of the relative optical air mass

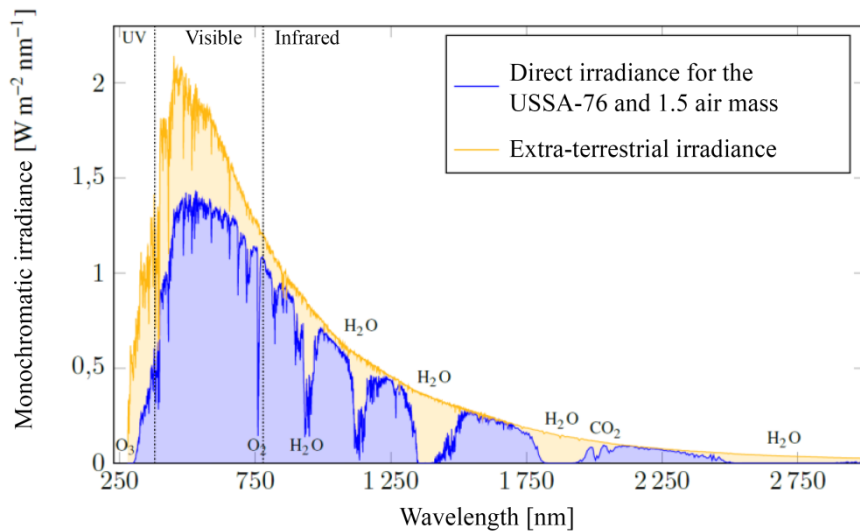


Figure 2.7. Spectral distribution of the extra-terrestrial irradiance and of the irradiance at the ground for a USSA-76 and a 1.56 air mass (NREL data, <https://www.nrel.gov/grid/solar-resource/spectra-am1.5.html>)

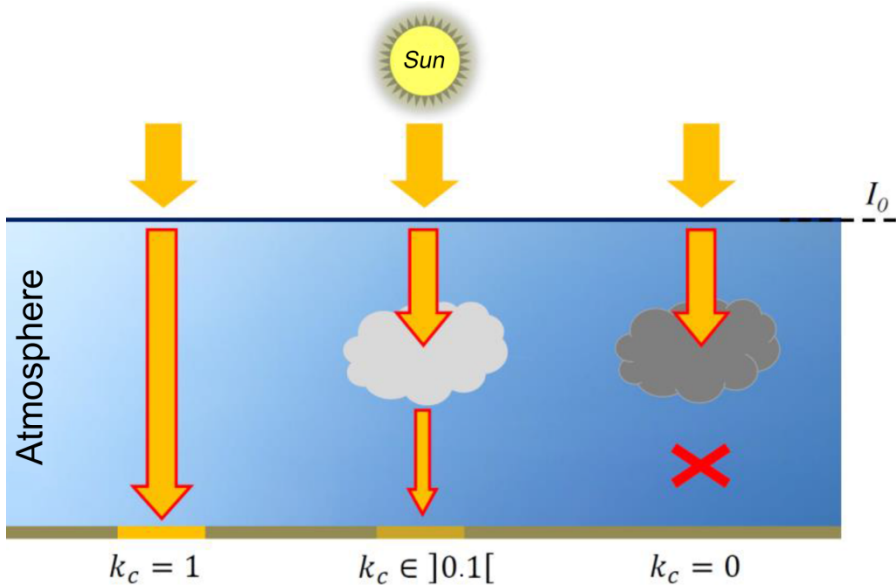


Figure 2.8. Schematic representation of the clear-sky index k_c

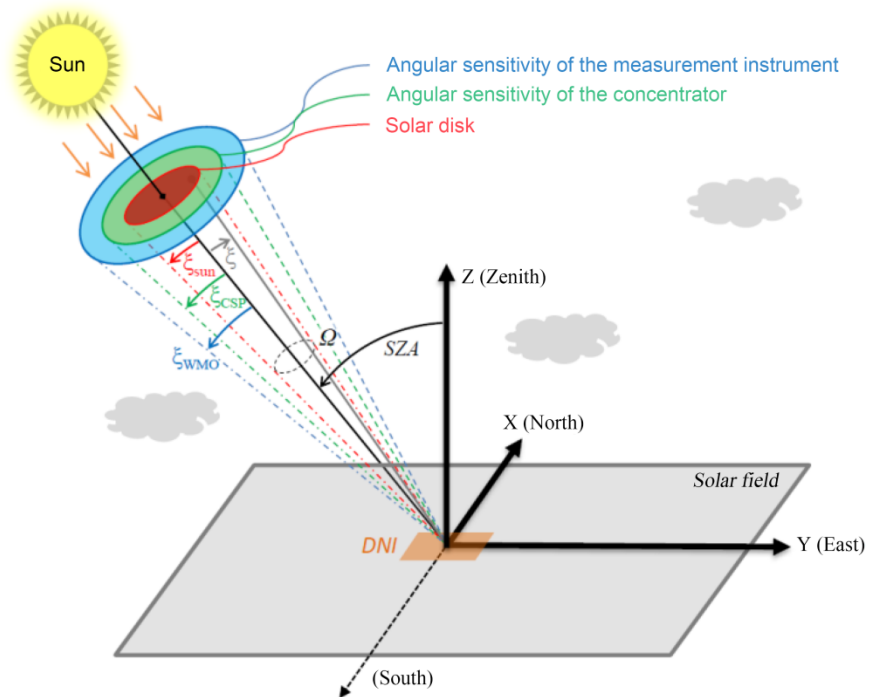


Figure 2.9. Schematic representation relative to DNI definition

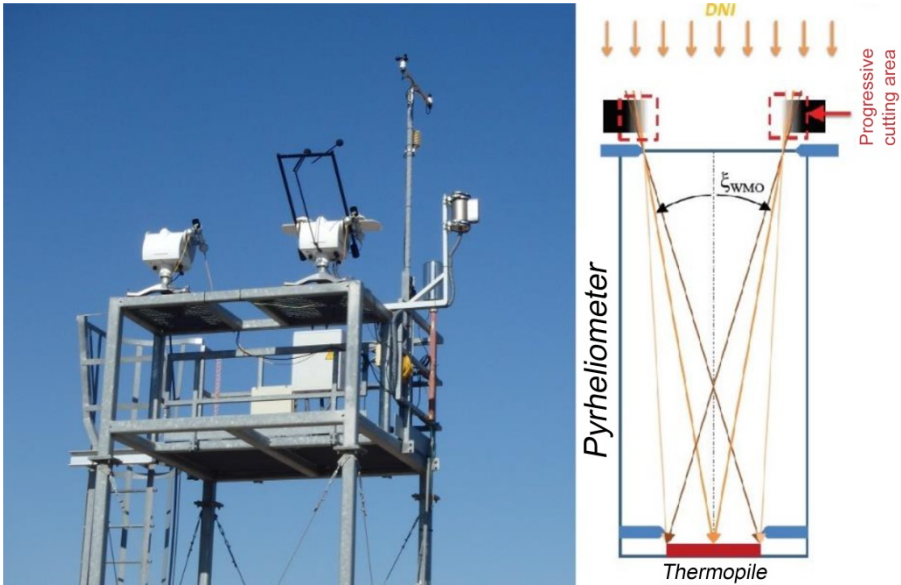


Figure 2.10. Left: image of two pyrheliometers on solar trackers. Right: diagram of a pyrheliometer



Figure 2.11. Two RSI installed at the PROMES-CNRS laboratory, Perpignan

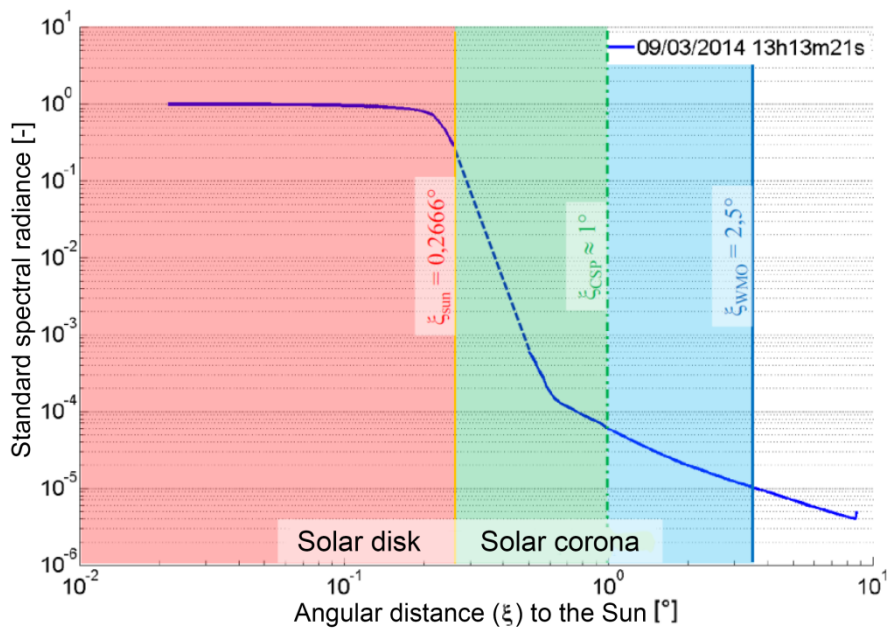


Figure 2.12. Example of the measurement of the solar profile using SAM (Odeillo)



a) SAM at PROMES-CNRS laboratory (Odeillo)
– Visidyne



b) BPI CSR 460 sensor (Wilbert 2014)
– Black Photon Instruments

Figure 2.13. Systems for the measurement of circumsolar irradiance

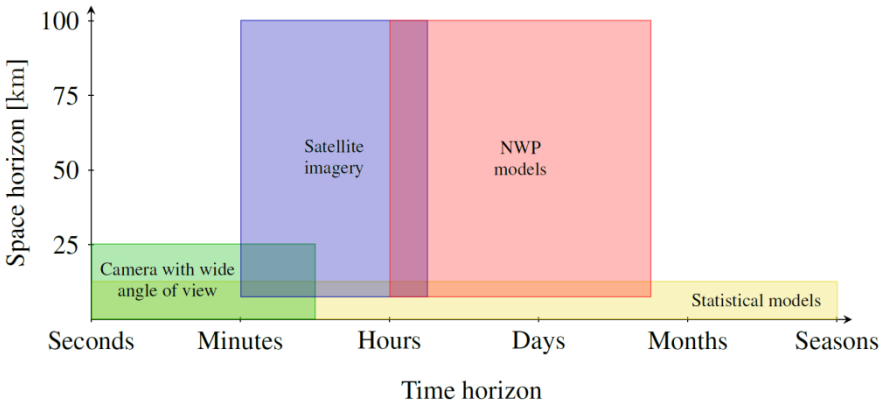


Figure 2.15. Approaches for solar resource forecasting, depending on the spatiotemporal horizon (adapted from Ramirez and Vindel 2017)

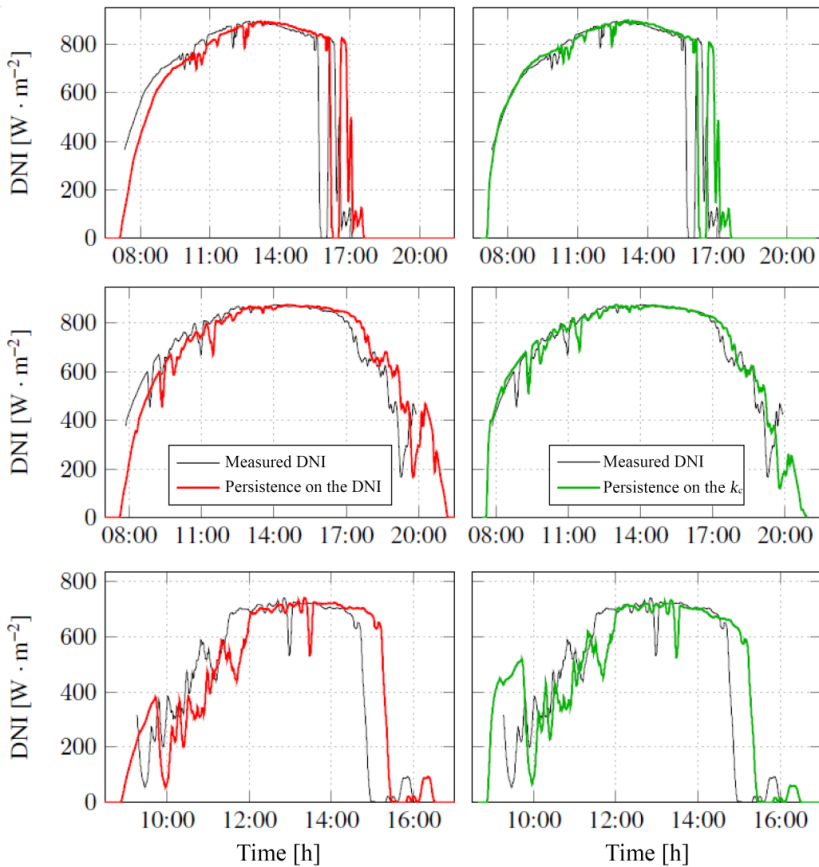


Figure 2.16. Forecasting examples at $\Delta t = 30 \text{ min}$ using DNI persistence (on the left) and clear-sky index k_c persistence (on the right), over three different days (sampling of measurements: 1 min)



Figure 2.17. The PROMES sky imager installed at Odeillo and several HDR images acquired (after tone correspondence)

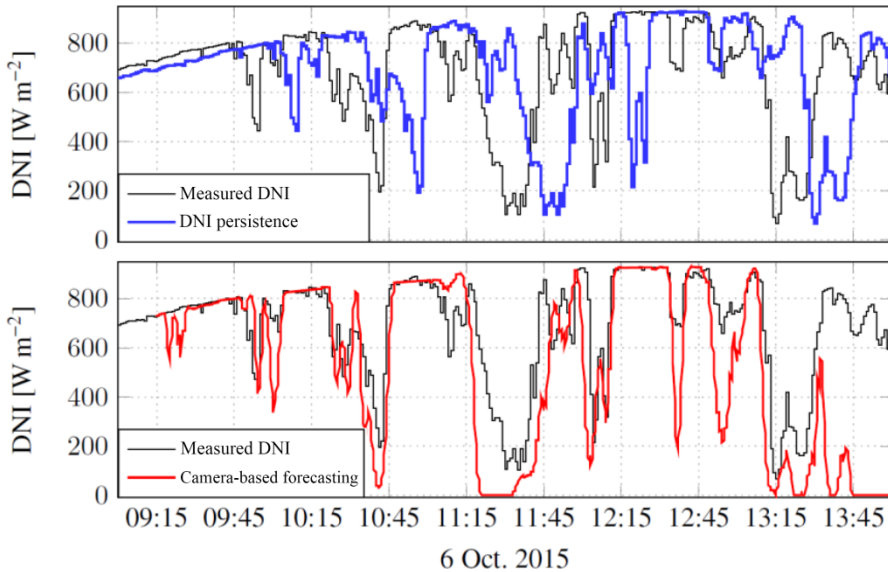


Figure 2.18. Forecasting examples of DNI at $\Delta t = 15 \text{ min}$, using a DNI persistence (upper image) and a sky imager (lower image), in the case of a good forecasting of the cloud motion (sampling of measurements: 1 min; temporal resolution step of the forecasting: 20 s)



Figure 3.1. Archimedes' Burning Mirrors, *fresque by Giulio Parigi (1571–1635), Uffizi Gallery, Florence*

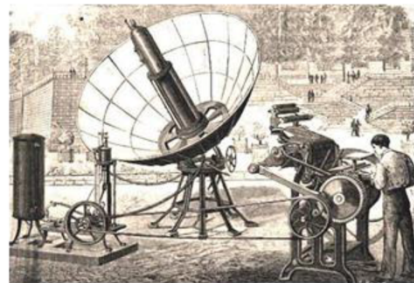
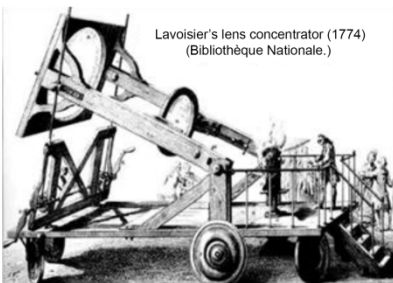
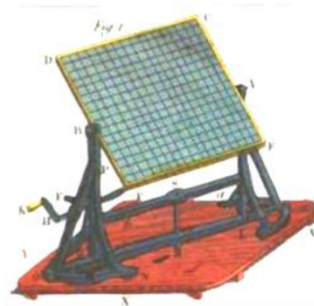
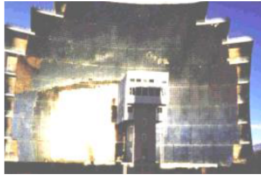


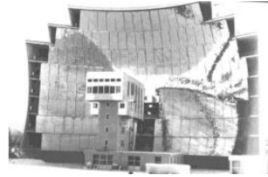
Figure 3.2. *The burning mirror of Louis XIV (upper left), the segmented concentrator of Buffon (upper right), the “water-based” concentrator of Lavoisier (lower left) and the steam engine of Augustin Mouchot (lower right)*



Overview



Parabolic concentrator



Parabolic concentrator



Parabolic concentrator



Flat heliostat



Field of flat heliostats

Figure 3.3. Large 1,000 kW solar furnace at Odeillo: overview, images of the parabolic concentrator and images of the field of flat heliostats



Overview



Tower view of the heliostat field
Photo Thémis Solaire Innovation



Receiver



Cethel focusing heliostat



Thek parabolic concentrators

Figure 3.5. The various components of Themis solar power tower

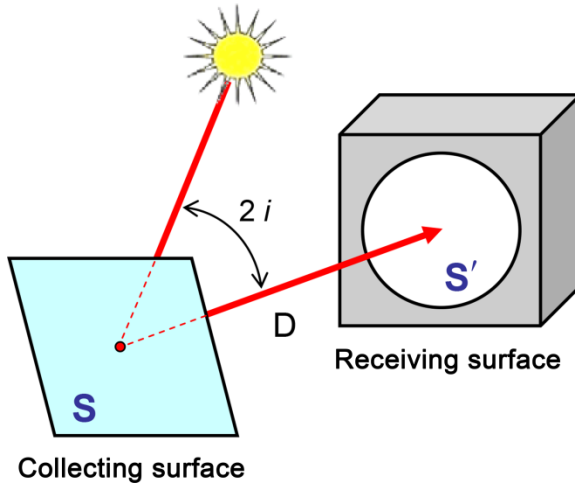


Figure 3.7. Fundamental parameters of the collecting and receiving surfaces

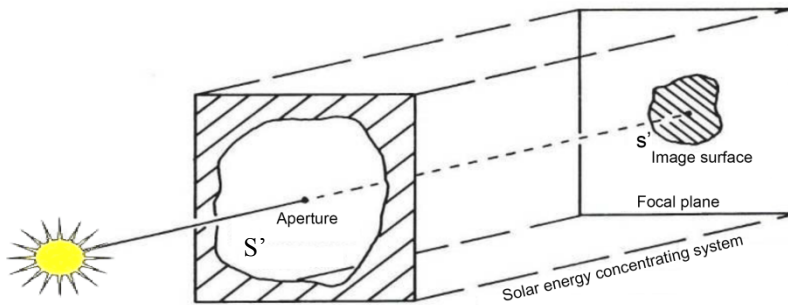


Figure 3.8. Definition of the concentration factor C with respect to the collecting and receiving surfaces

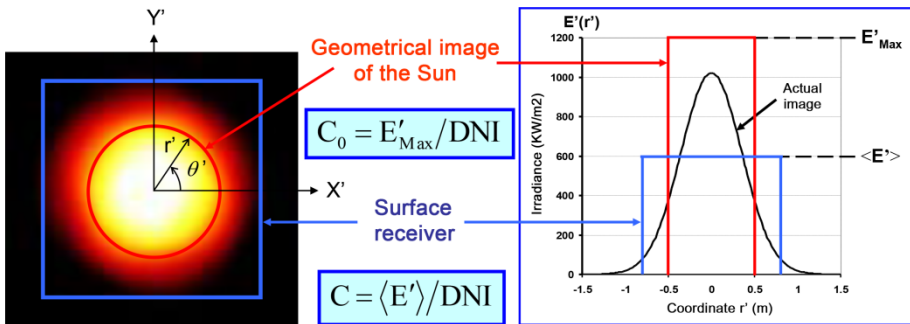


Figure 3.9. Definition of the concentration factor C using the ratio of irradiances

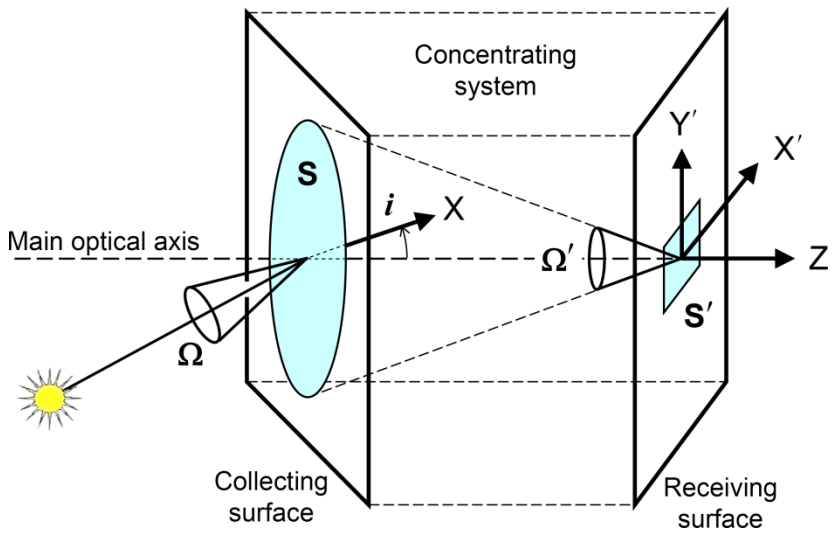


Figure 3.10. Definition of the concentration factor C by the ratio of solid angles

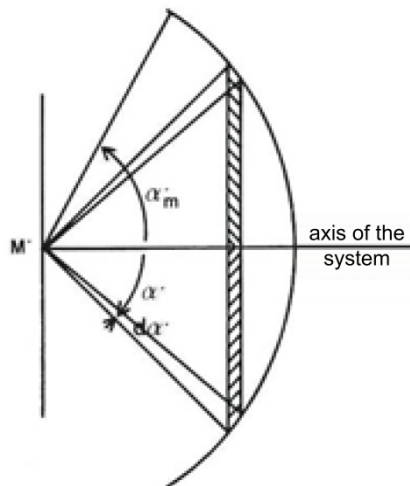


Figure 3.11. Calculation of the maximal irradiance at the focal point of a concentrator

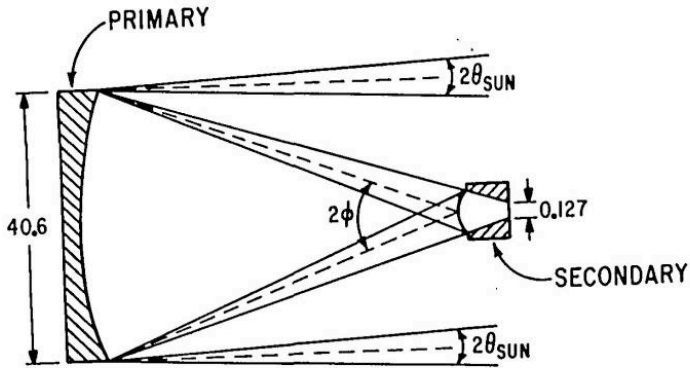


Figure 3.12. Two-stage energy concentrating system (Gleckman 1988)

- δ_s Local surface errors
- δ_m Microscopic surface (roughness) errors
- δ_p Global pointing error of a heliostat
- δ_r Adjustment error of a segment or individual module

$$\delta_{\text{Tot}} \approx \sqrt{\delta_s^2 + \delta_r^2 + \delta_p^2}$$

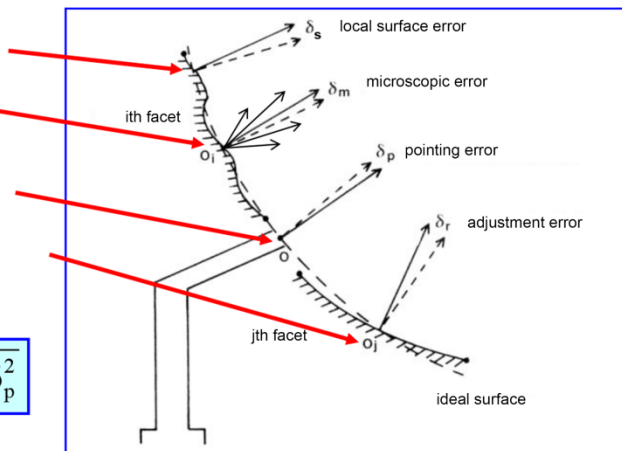
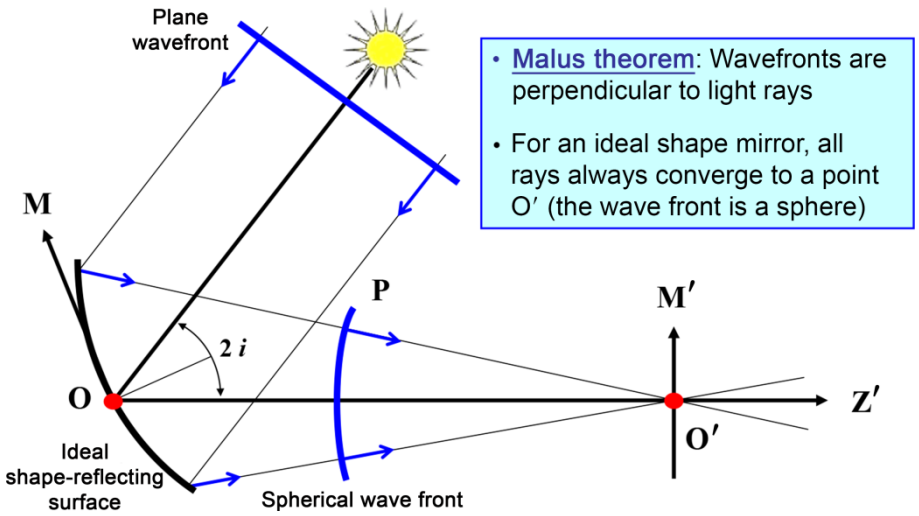
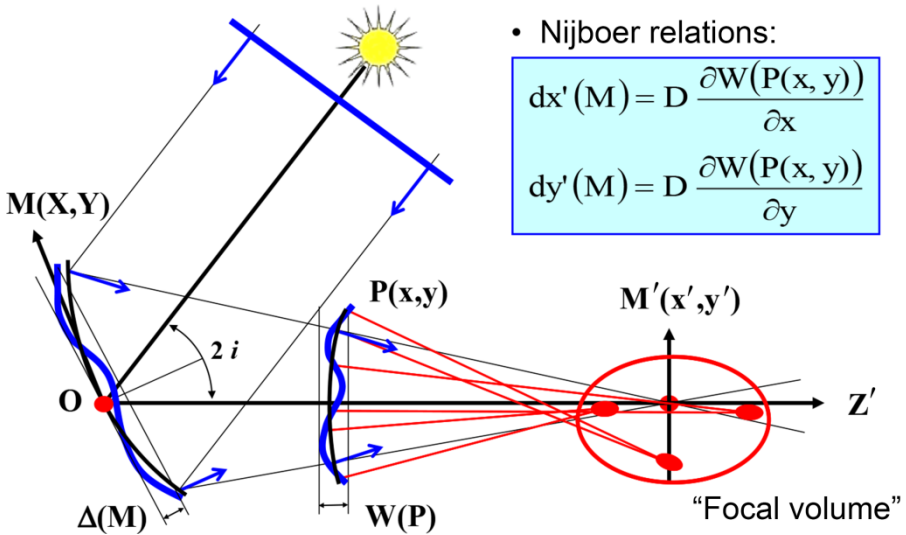


Figure 3.13. Error sources specific to solar concentrators



- **Malus theorem:** Wavefronts are perpendicular to light rays
- For an ideal shape mirror, all rays always converge to a point O' (the wave front is a sphere)



- Nijboer relations:
- $$dx'(M) = D \frac{\partial W(P(x, y))}{\partial x}$$
- $$dy'(M) = D \frac{\partial W(P(x, y))}{\partial y}$$

Figure 3.14. Wave fronts reflected by an ideal shape mirror (upper image) and an actual concentrator (lower image)

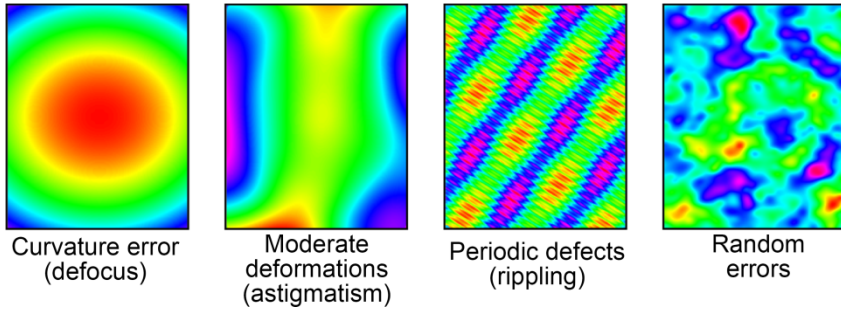


Figure 3.15. False color representation of various types of local surface errors

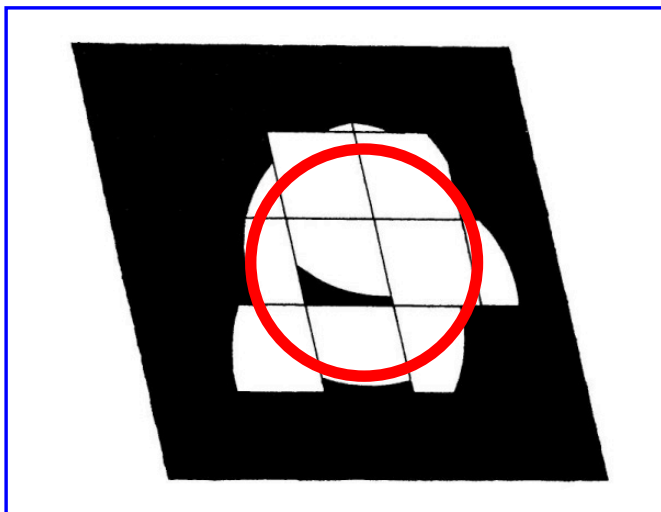


Figure 3.16. Visualization of the adjustment errors of a flat heliostat (Hénault 1989)

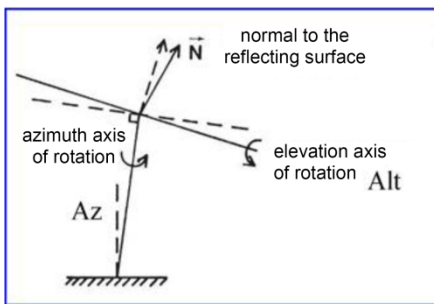


Figure 3.17. Illustration of the open-loop control mode (on the left) or closed-loop control mode (on the right)

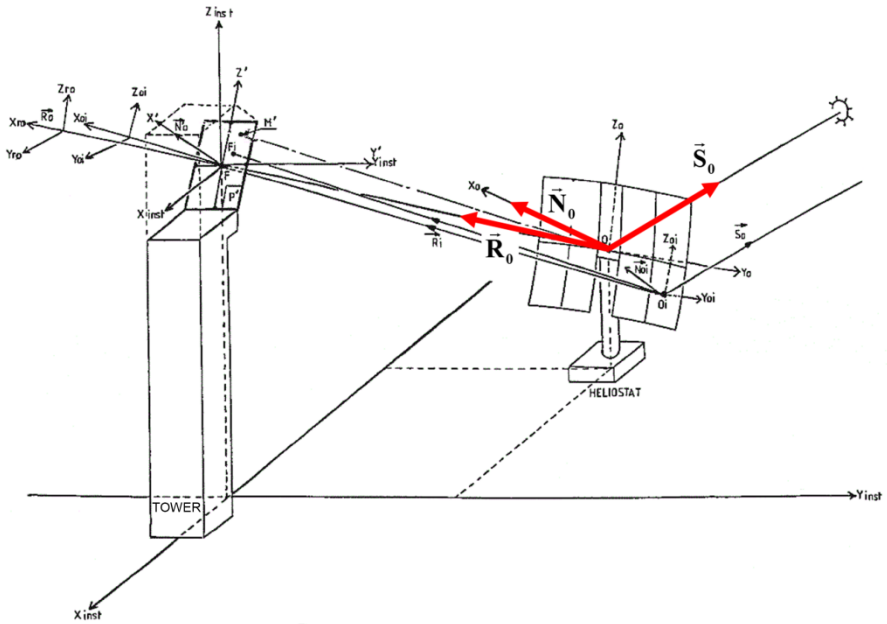


Figure 3.18. Open-loop control of a heliostat of a tower power plant

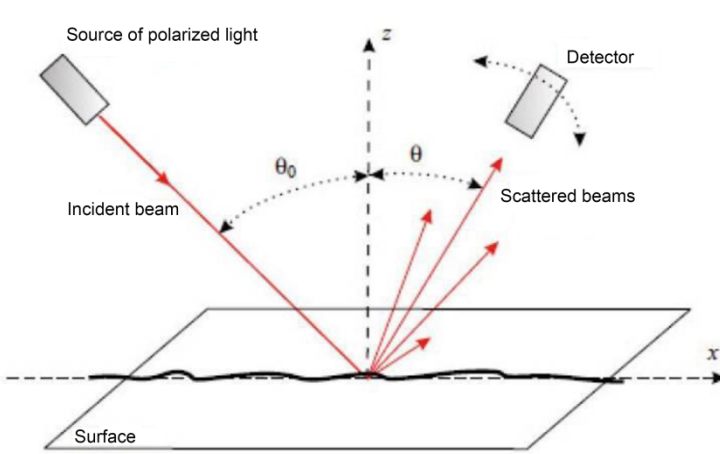


Figure 3.19. Microscopic surface errors and their measurement means (Silvestri et al. 2010)

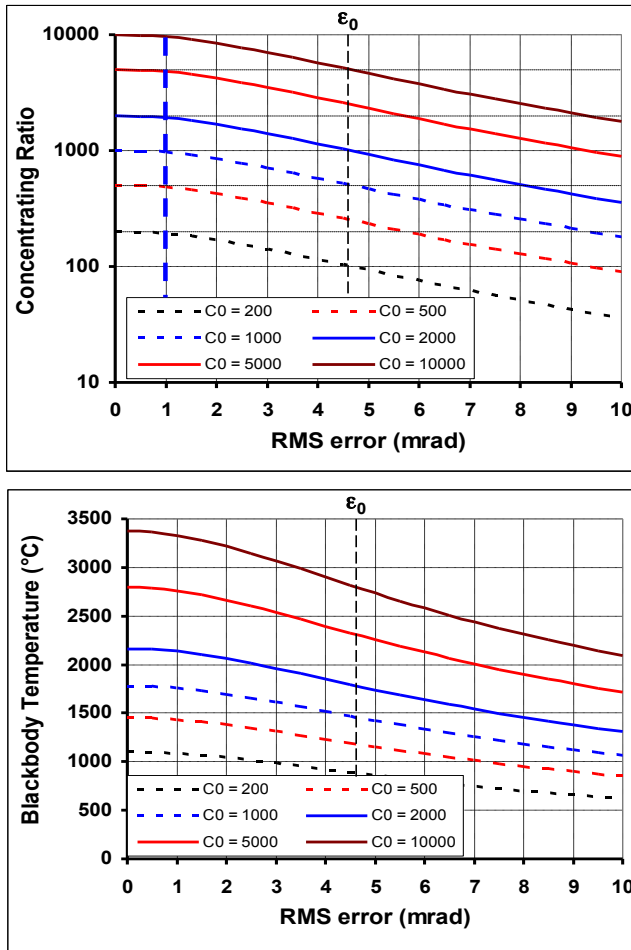


Figure 3.20. Concentration and temperature error depending on angular errors δ (Hénault 2015)

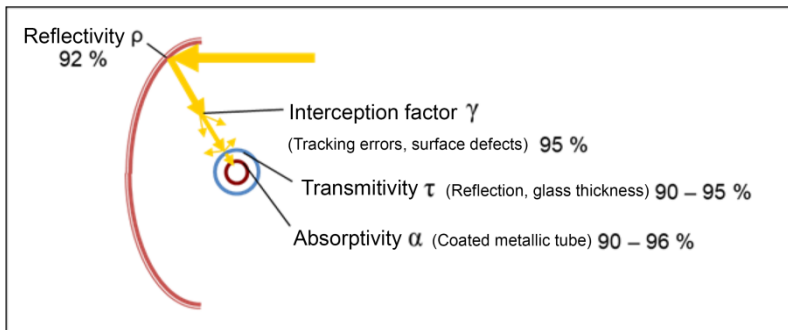


Figure 3.21. Schematic representation of the physical phenomena affecting global optical efficiency

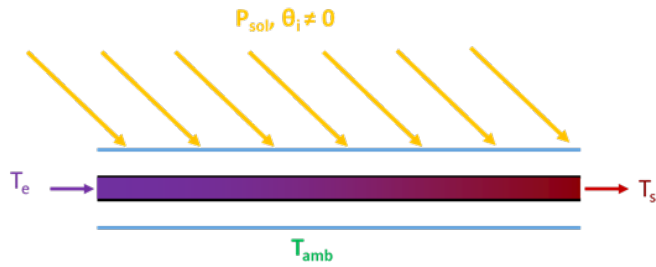


Figure 3.22. Optical qualification test, evaluation of k_{θ} (Fasquelle et al. 2017)

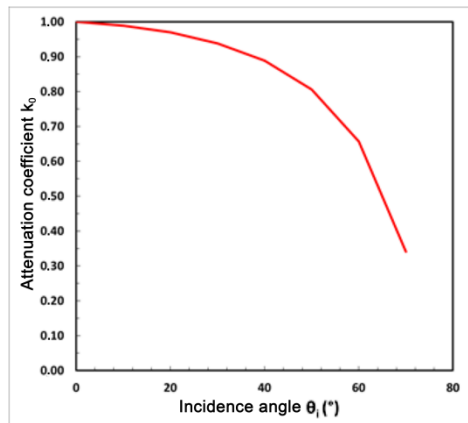


Figure 3.23. Example of optical qualification (Valenzuela et al. 2014)

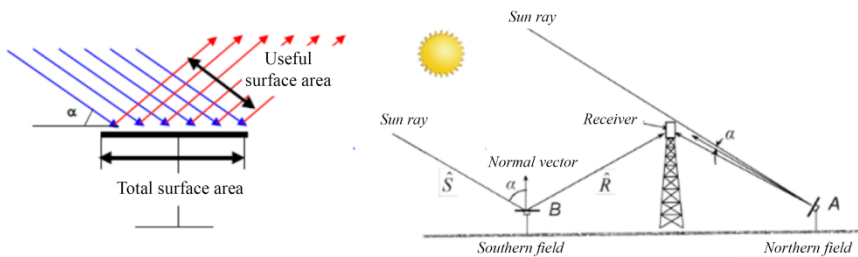


Figure 3.25. Schematic representation of optical losses due to cosine effect

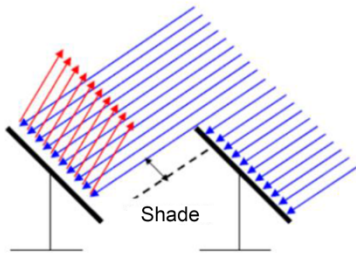


Figure 3.26. *Optical losses due to shading*

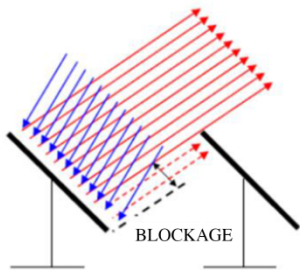


Figure 3.27. *Optical losses by blocking*

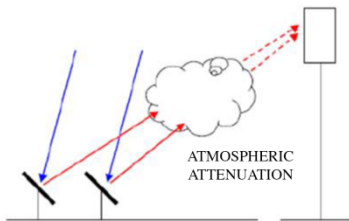


Figure 3.28. *Optical losses due to atmospheric attenuation*

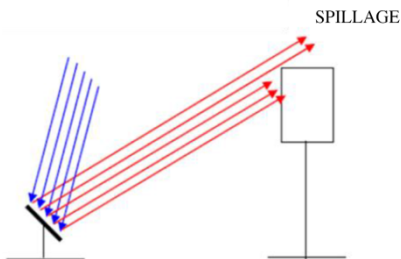


Figure 3.29. *Optical losses due to spillage*

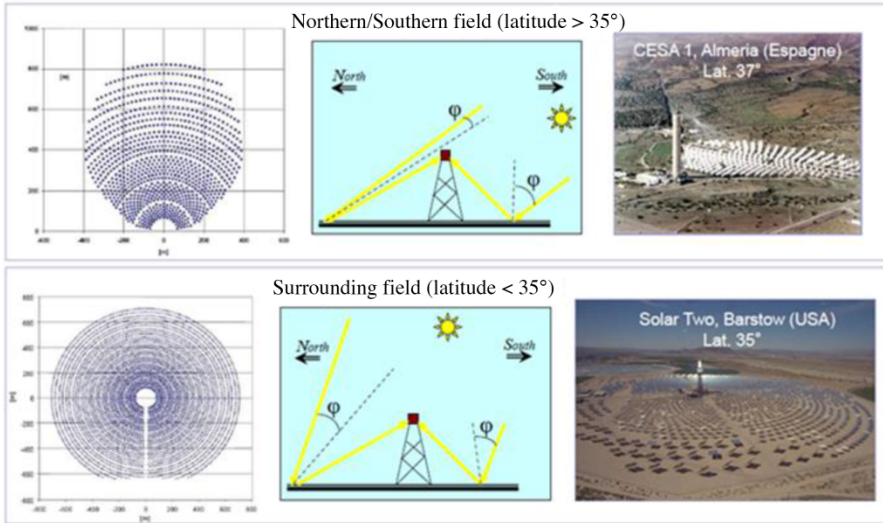


Figure 3.30. Northern/Southern fields and surrounding fields

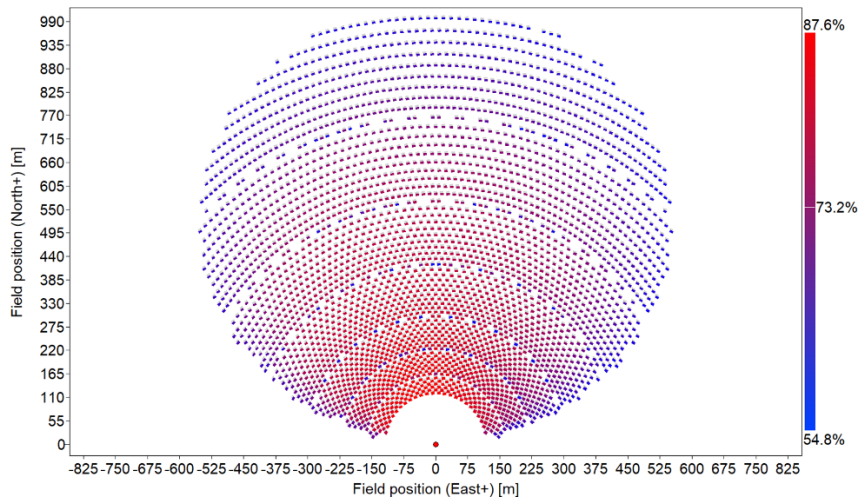


Figure 3.32. Heliostat field simulated by SolarPILOT software for a 100 MWth average power incident on the solar receiver. The tower height is 120 m, and the surface area of heliostats is 49 m². The right scale reflects the optical efficiency of heliostats

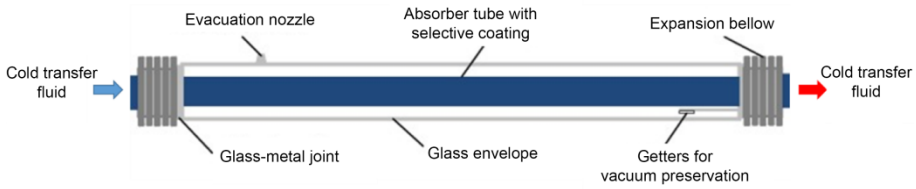


Figure 4.1. Schematic representation of an absorber tube and its components (Espinosa-Rueda et al. 2016)

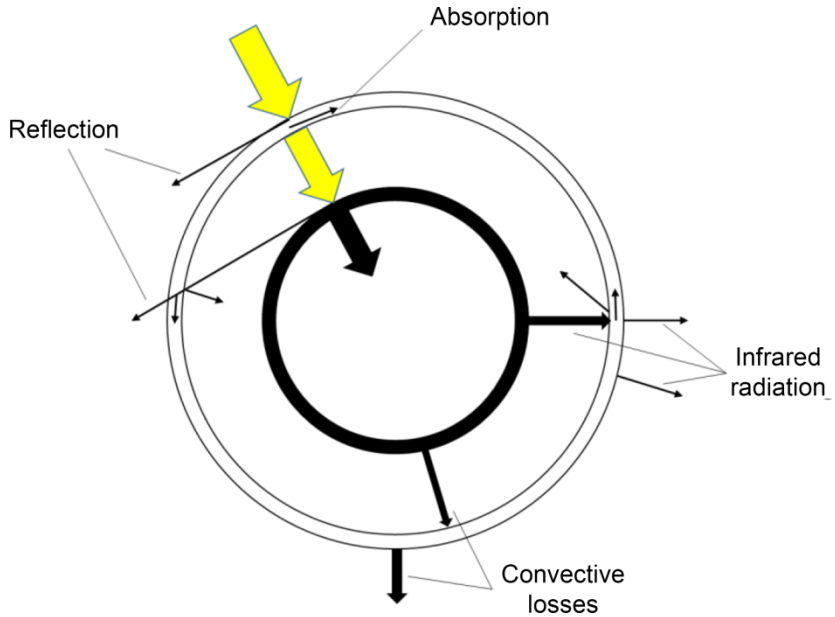


Figure 4.2. Thermal phenomena in an absorber tube

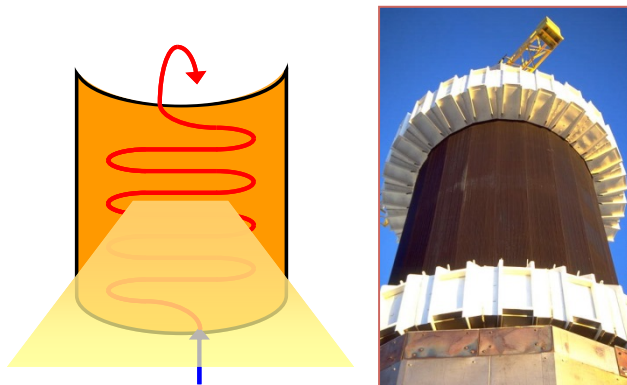


Figure 4.4. Diagram and image of a circular flat receiver

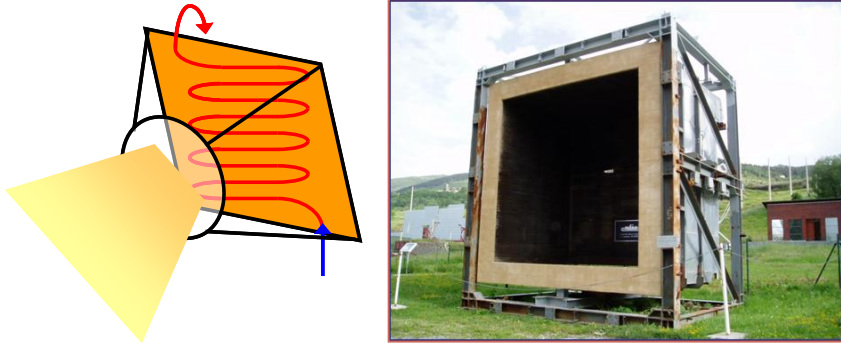


Figure 4.5. Diagram and image of a cavity receiver

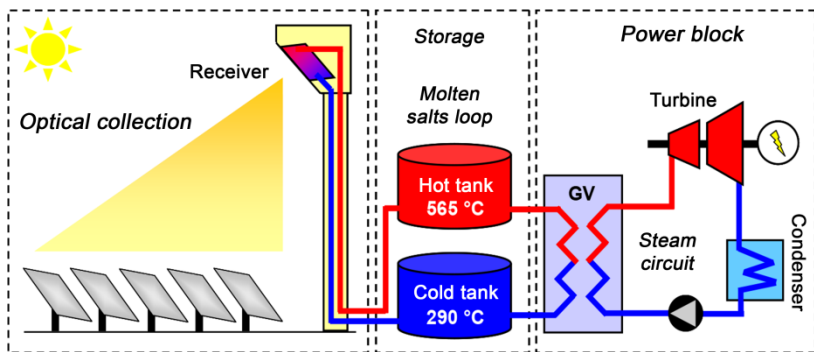


Figure 4.6. Schematic diagram of a tower power plant using molten salt as the heat transfer fluid (Grange 2012)



Figure 4.7. Gemasolar, tower power plant with molten salt near Seville, Spain (Ho 2017)

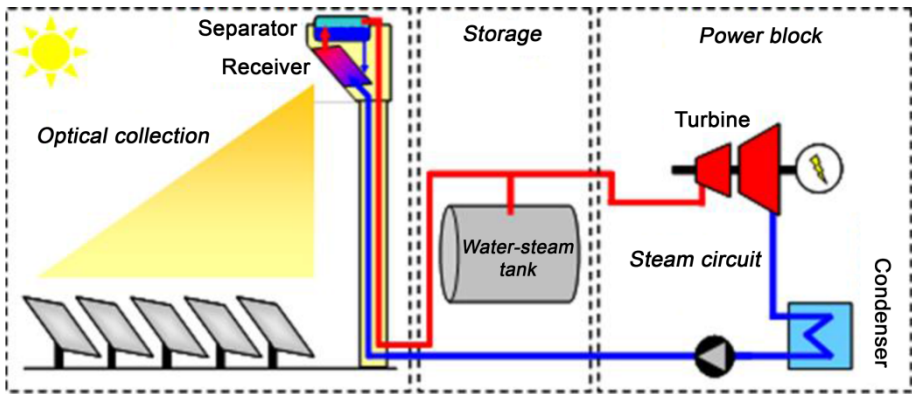


Figure 4.8. Schematic diagram of a tower power plant with water–steam as the heat transfer fluid (Grange 2012)



Figure 4.9. PS10 (left) and PS20 (right) near Seville, Spain



Figure 4.10. Ivanpah tower power plant (Ho 2017)

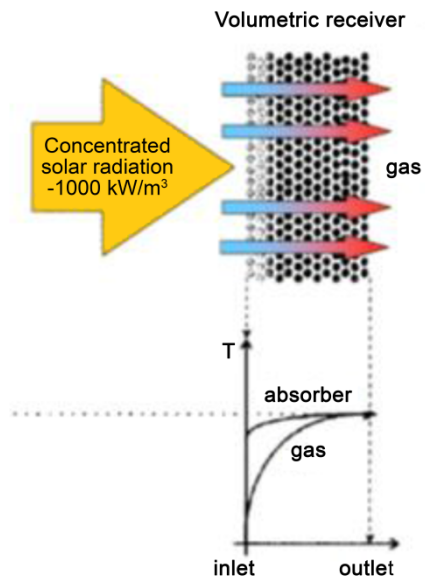


Figure 4.11. Schematic representation of a receiver (Grange 2012)

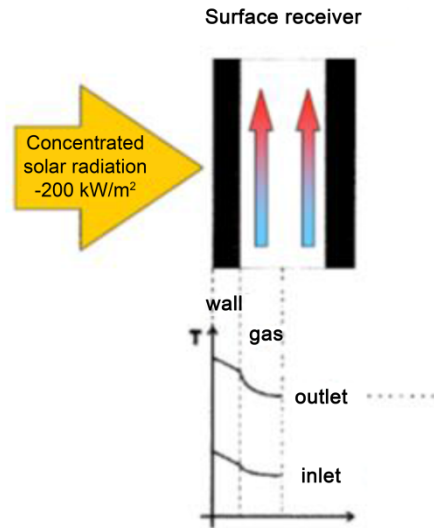


Figure 4.12. Schematic representation of a surface receiver (Grange 2012)

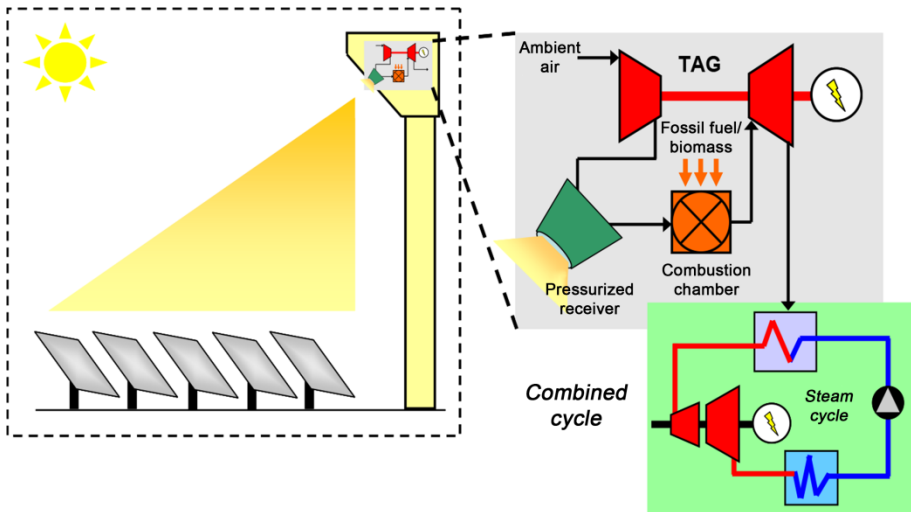


Figure 4.13. Schematic diagram of a tower power plant with pressurized air as the heat transfer fluid coupled with a gas turbine (Grange 2012)

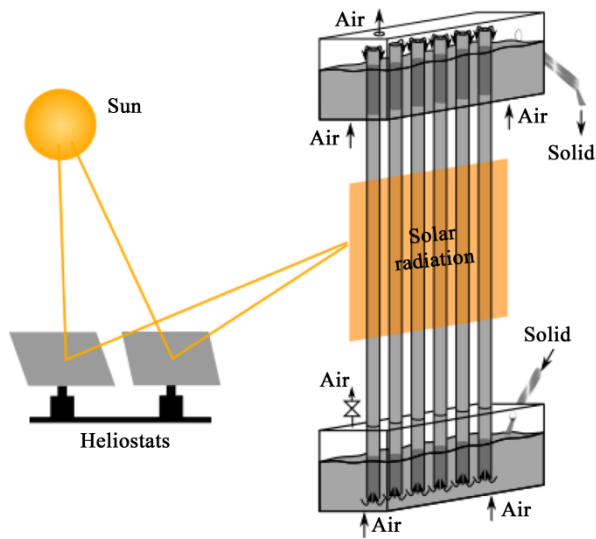


Figure 4.14. Principle of a solar receiver with the vertical transport of dense fluidized gas-particle suspension subjected to concentrated solar radiation (Boissière 2015)



Figure 4.15. Images of inserts allowing the increase in the residence time of the particles subjected to concentrated solar radiation (Ho et al. 2017)

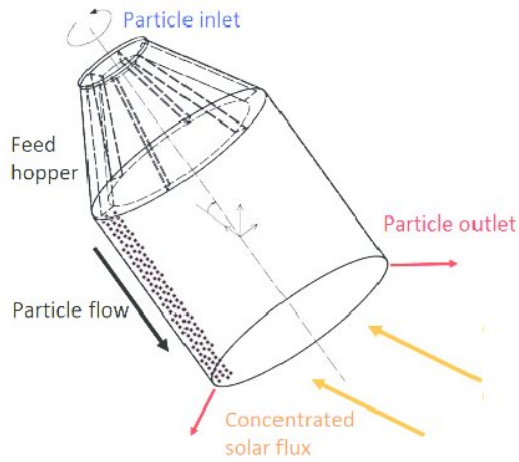


Figure 4.16. Principle of the centrifugal particle receiver (Prosin 2015)

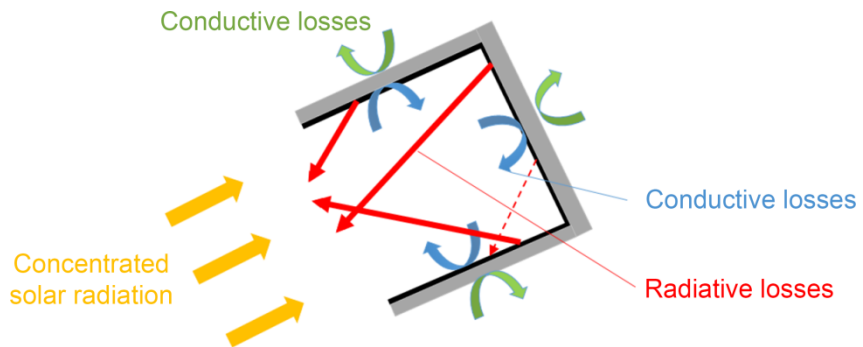


Figure 4.17. Schematic representation of thermal losses in a solar cavity receiver

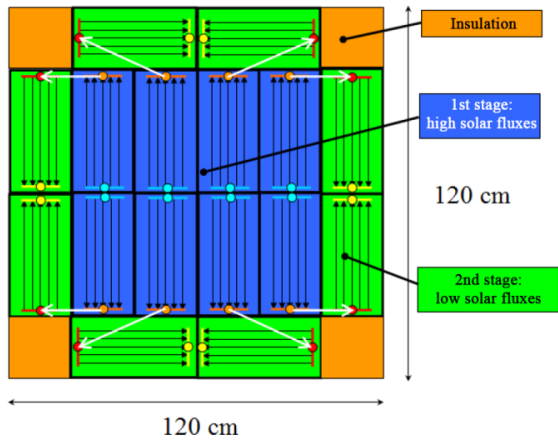


Figure 4.22. Air flow in the absorber modules (Grange 2012)

					526	562	774	803	841	869	871	842	804	769	562	507
					607	700	730	753	780	807	809	776	748	723	681	584
					712		736		852		844		761		723	
					697		634		741		703		645		669	
					754		737		851		847		751		769	
					686		592		654		646		598		699	
					785		718		833		806		726		810	
					716		536		580		571		540		732	
					822		669		775		758		678		839	
					748		470		492		489		472		755	
					815		681		765		775		680		816	
					738		472		490		492		472		738	
					774		696		794		788		715		771	
					705		533		570		570		537		705	
					738		715		808		805		727		736	
					675		584		636		635		591		676	
					702		722		804		805		728		697	
					648		624		684		684		631		651	
					605	662	749	777	806	835	830	805	776	743	653	592
					566	616	704	726	751	777	774	749	725	702	570	549

Figure 4.23. Mapping of wall temperatures (upper part in black) and outgoing air temperatures (lower part in red) for each element of the discretization. Air flow is symbolized by arrows; temperatures in °C (Grange 2012)

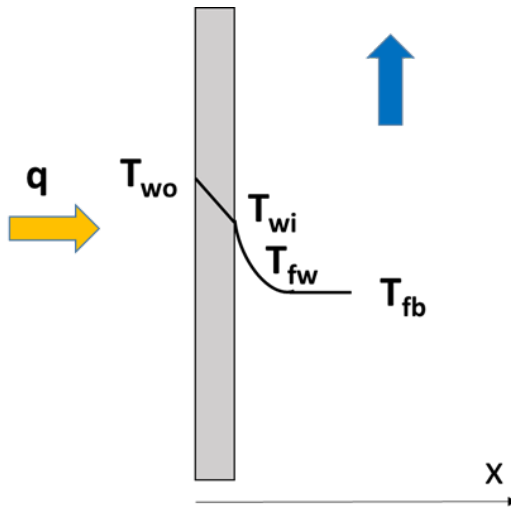


Figure 5.1. Schematic representation of the continuity of the heat flux at the fluid–wall interface in 1D geometry

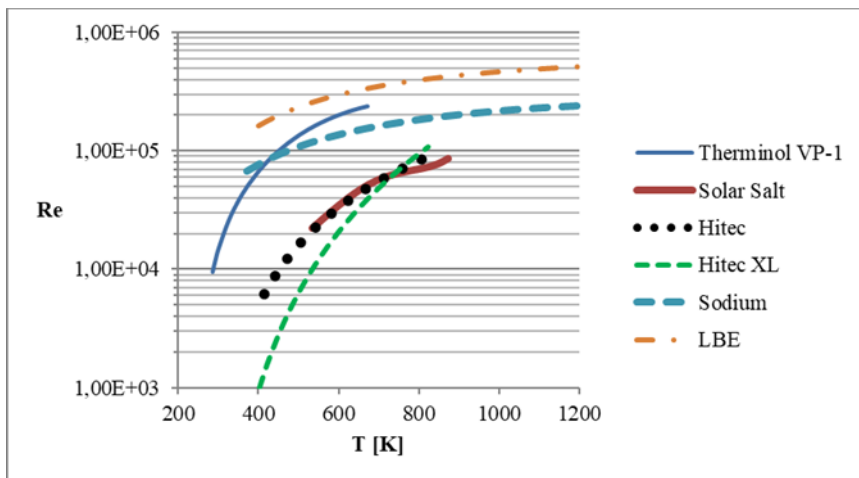


Figure 5.4. Reynolds number depending on the temperature for liquid heat transfer fluids flowing at 2 m/s in a tube receiver (Benoit et al. 2016)

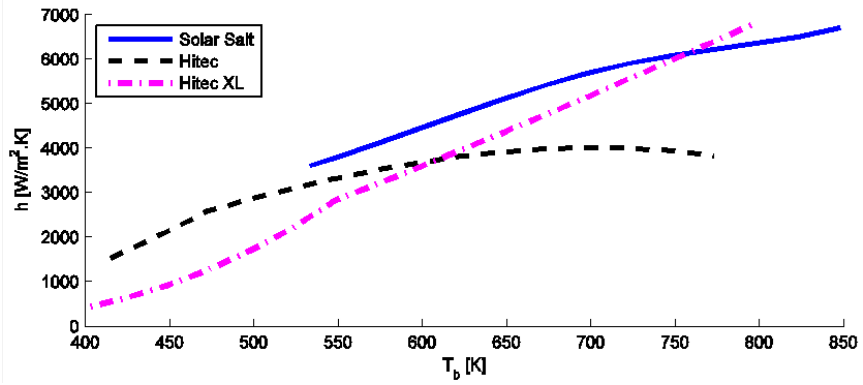


Figure 5.6. Fluid–wall heat transfer coefficients for molten salts (2 m/s)

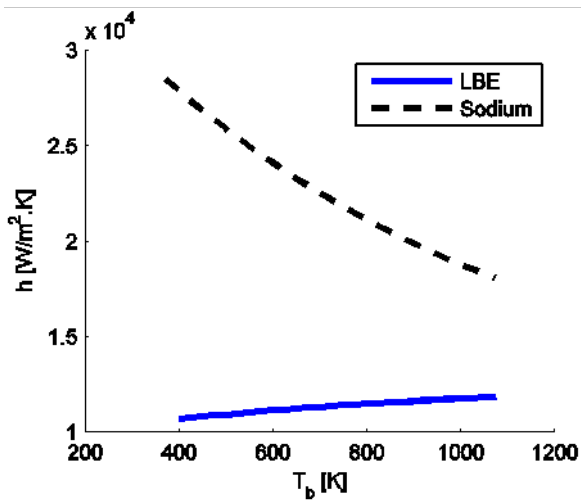


Figure 5.7. Fluid–wall heat transfer coefficients for liquid metals (2 m/s)

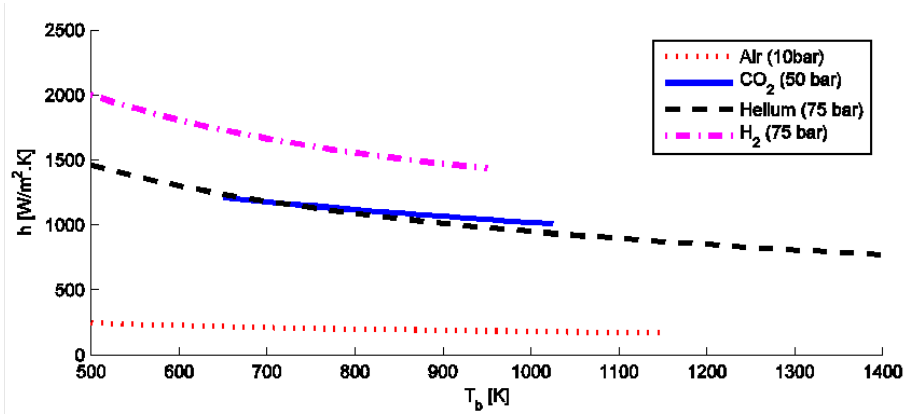


Figure 5.8. Fluid–wall heat transfer coefficients for gases (15 m/s)

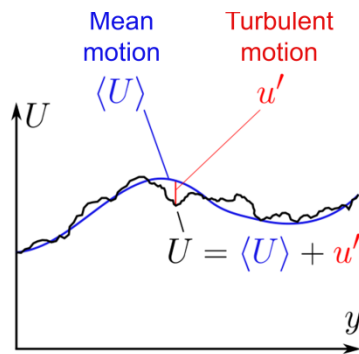


Figure 6.1. Schematic representation of the profiles of mean and fluctuating fields

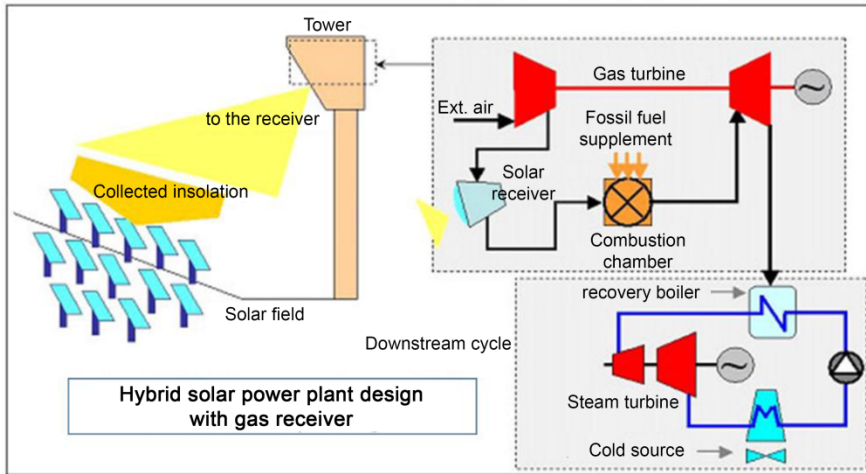


Figure 6.2. Schematic representation of a hybrid solar power plant with combined cycle employing a solar receiver with pressurized air. The air is compressed by the compressor of the gas turbine

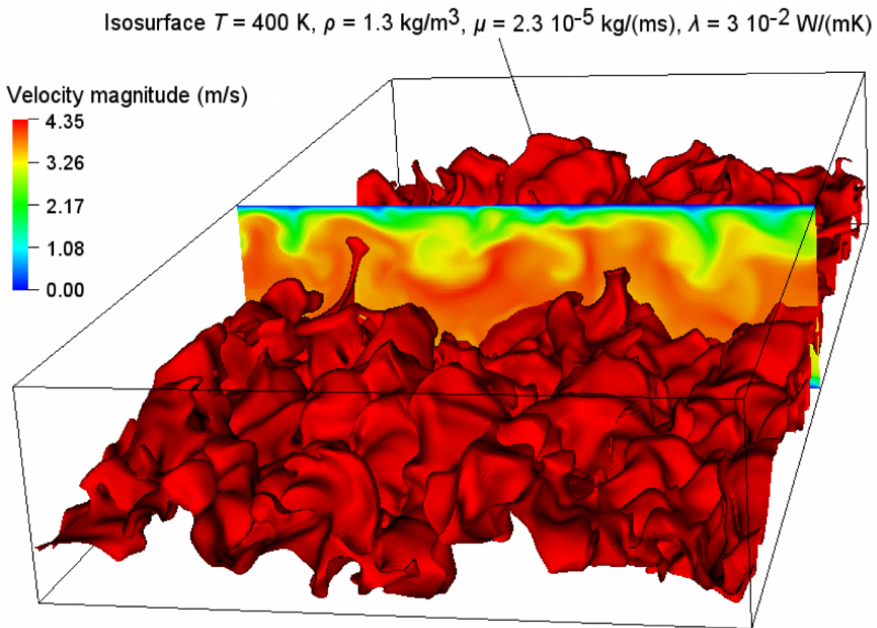


Figure 6.3. Illustration of dynamic and thermal fields in a solar receiver (isosurface $T = 400 \text{ K}$)

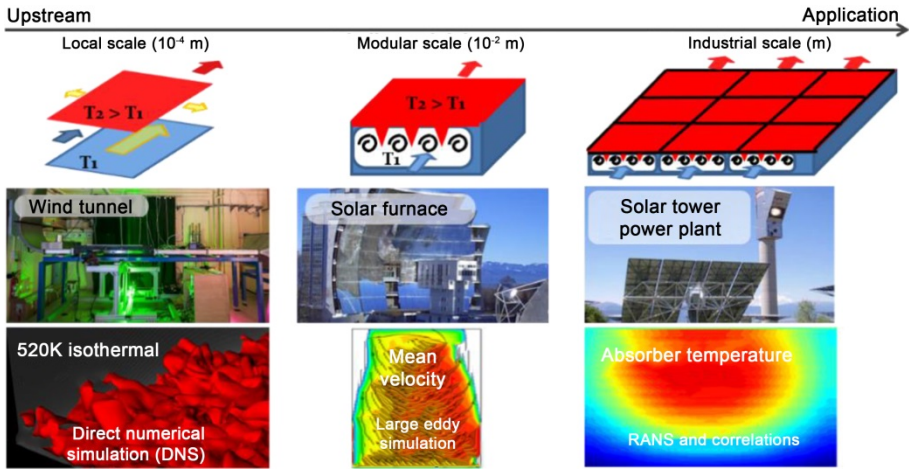


Figure 6.4. The various modeling approaches for the numerical study of flows and heat transfers in solar receivers

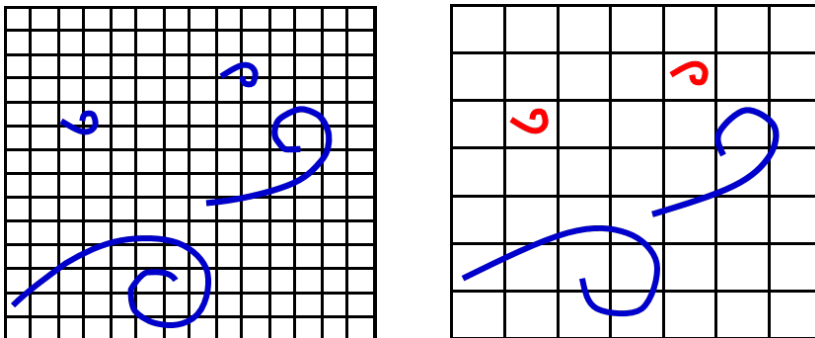


Figure 6.5. Schematic representation of DNS strategies (left) and LES strategies (right). The blue turbulent structures are resolved, and the red ones are not resolved. In direct numerical simulation, all the structures are resolved (grid on the left). In large-eddy simulation, only the large structures are resolved (grid on the right)

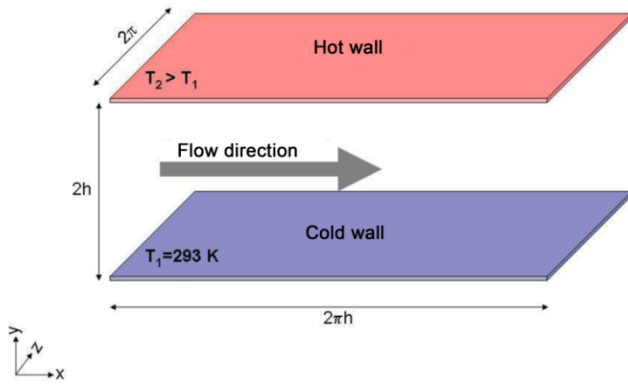


Figure 6.9. Simplified geometry of a solar receiver

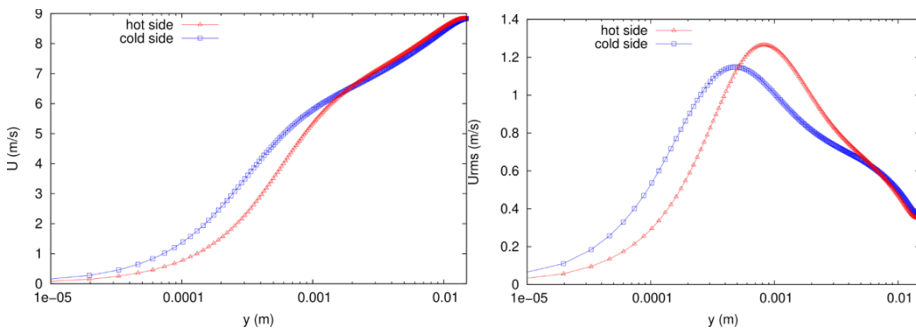


Figure 6.10. Profiles of longitudinal velocity (top) and of the standard deviation of longitudinal velocity (bottom) at the hot and cold sides of the channel resulting from the direct numerical simulation

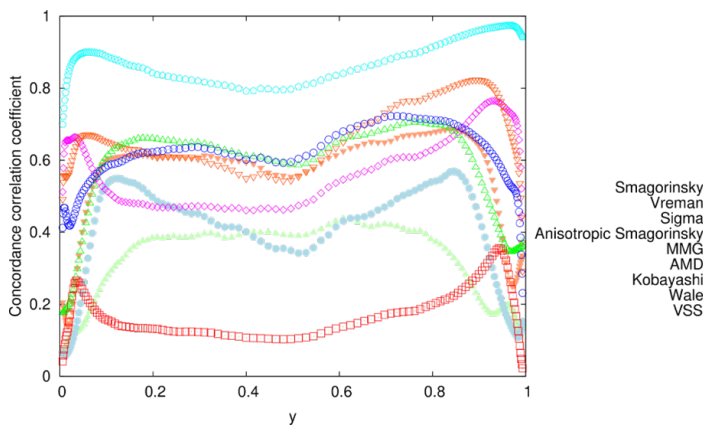


Figure 6.11. Coefficient of concordance between the exact subgrid-scale dissipation and the subgrid-scale dissipation corresponding to various models of the subgrid-scale tensor τ

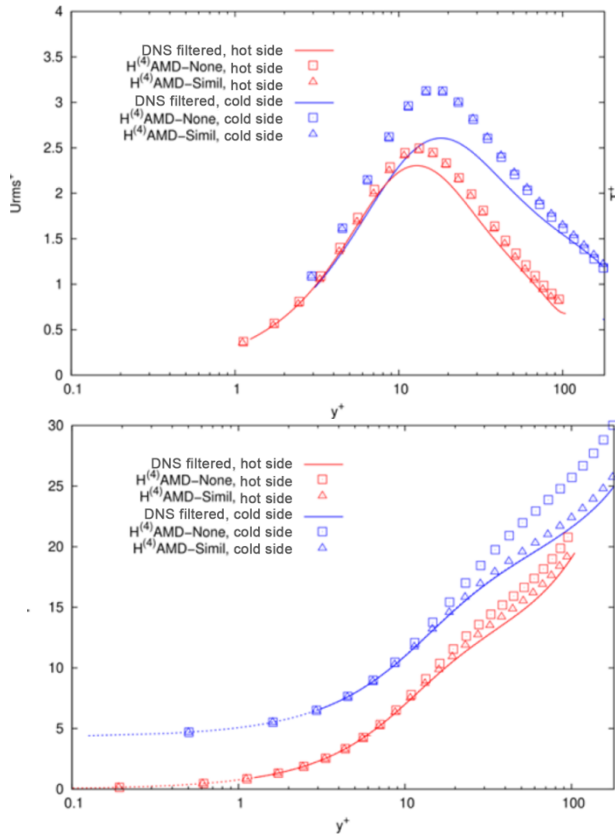


Figure 6.12. Standard deviation profiles for longitudinal velocity (top) and average temperature at the hot and cold sides of the channel resulting from the direct numerical simulation (filtered) and large-eddy simulations with or without modeling of the subgrid-scale vector π

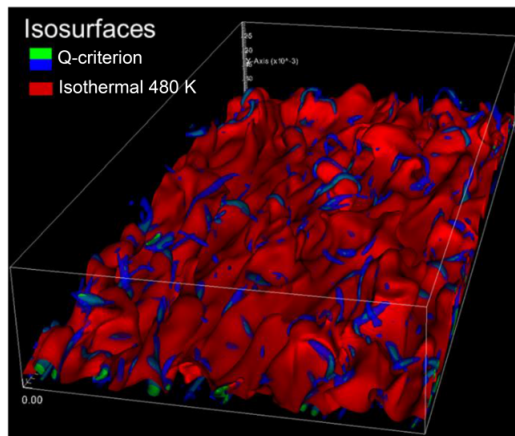


Figure 6.14. Illustration of turbulence/temperature interactions. Pressurized gas, bi-periodic channel with dissymmetric heating

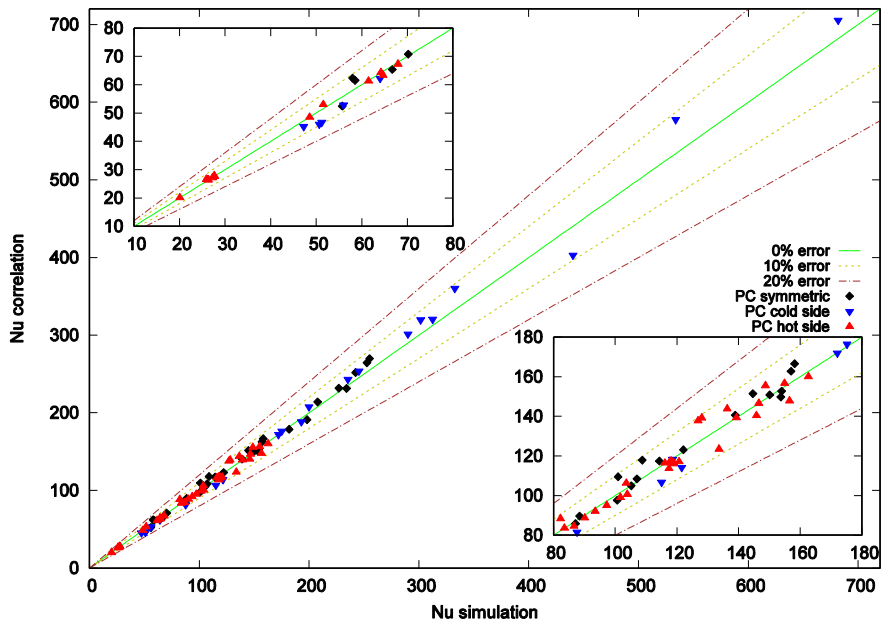


Figure 6.15. Comparison of Nusselt numbers obtained by the proposed correlation and by reference simulations

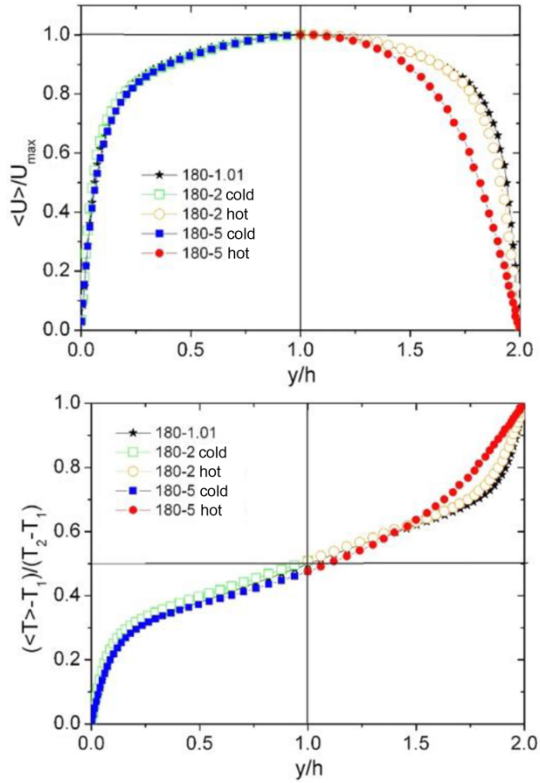


Figure 6.16. Evolution of the profiles of average velocity (top) and temperature (bottom) with the increase in the temperature ratio ($T_2/T_1 = 1.01; 2$ or 5) and friction Reynolds number $Re_\tau = 180$

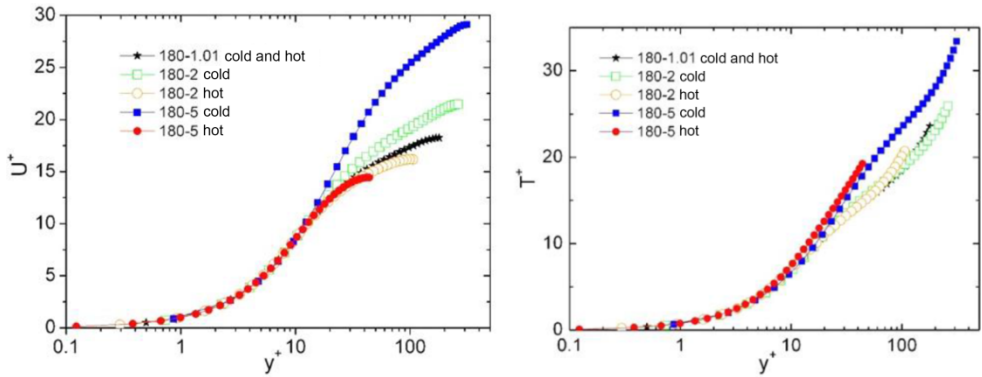


Figure 6.17. Comparison of the profiles of velocity (top) and temperature (bottom) at the hot and cold sides for various temperature ratios. The velocity and temperature are scaled by the friction velocity and temperature

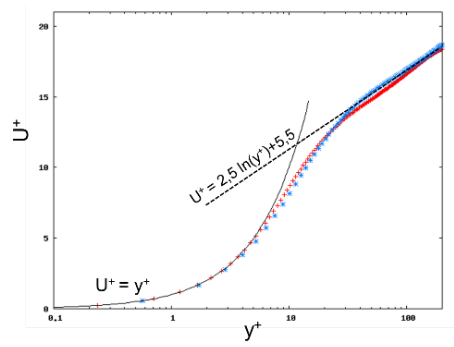


Figure 6.18. Longitudinal average velocity with the scaling of Van Driest

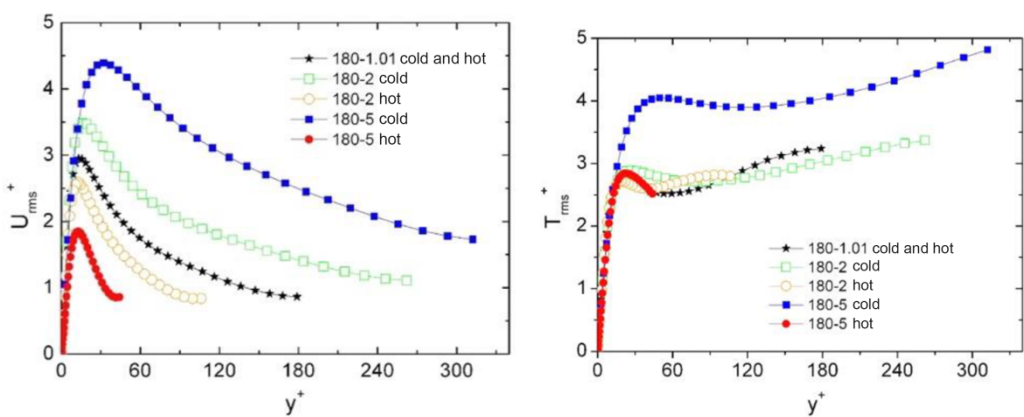


Figure 6.19. Standard deviation of velocity (top) and temperature (bottom) for various temperature ratios (1.01; 2 and 5) and a friction Reynolds number $Re_\tau = 180$

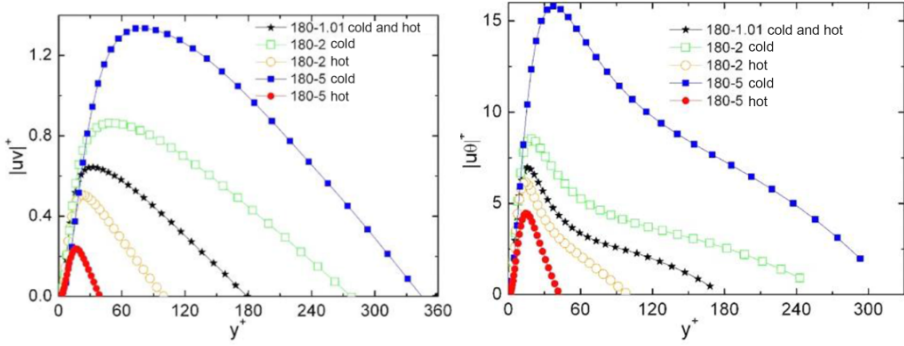


Figure 6.20. Correlations between longitudinal velocity and velocity normal to the walls on the left and between longitudinal velocity and temperature on the right for various temperature ratios

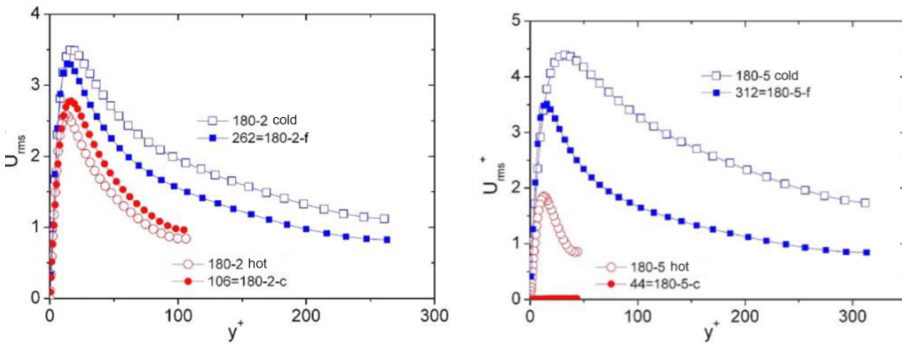


Figure 6.21. Comparison of the standard deviation of velocity under isothermal and strongly anisothermal configurations. On the left: temperature ratio of 2; on the right: temperature ratio of 5

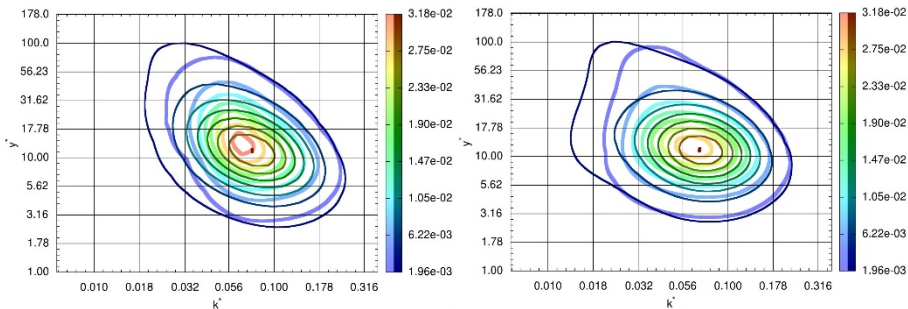


Figure 6.23. Spectrum of the production with semi-local scaling at $Re_\tau = 180$ (thick lines, light color) and $Re_\tau = 395$ (fine lines, dark color)

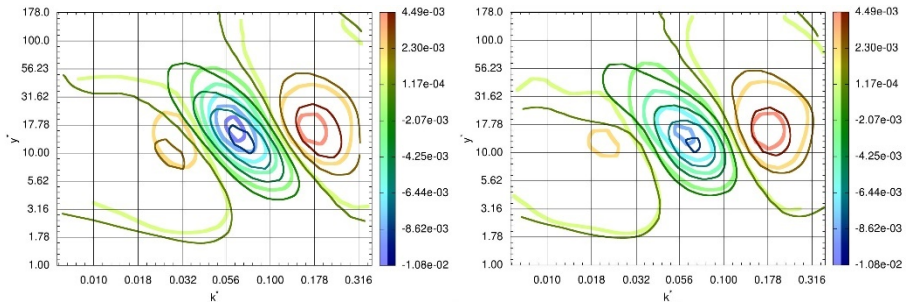


Figure 6.24. Spectrum of the interscale transfer with semi-local scaling at $Re_\tau = 180$ (thick lines, light color) and $Re_\tau = 395$ (fine lines, dark color)

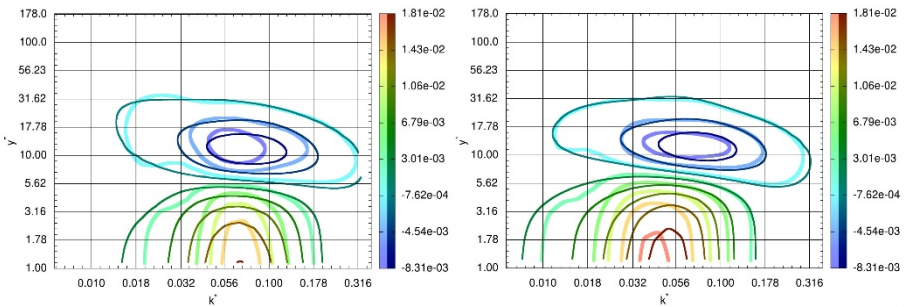


Figure 6.25. Spectrum of the spatial transfer with semi-local scaling at $Re_\tau = 180$ (thick lines, light color) and $Re_\tau = 395$ (fine lines, dark color)

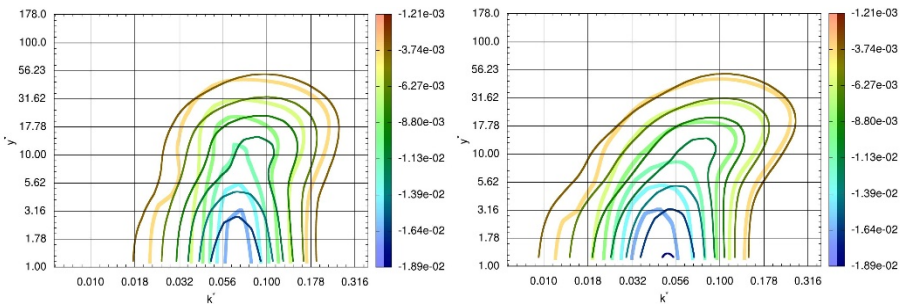


Figure 6.26. Spectrum of the interaction with internal energy with semi-local scaling at $Re_\tau = 180$ (thick lines, light color) and $Re_\tau = 395$ (fine lines, dark color)

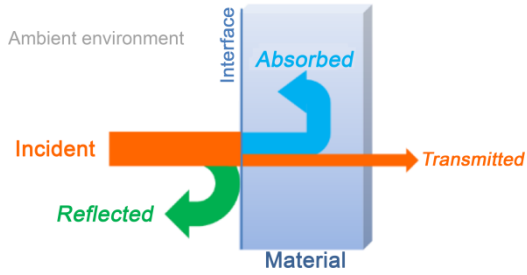


Figure 7.1. Interaction between an incident radiation and a material

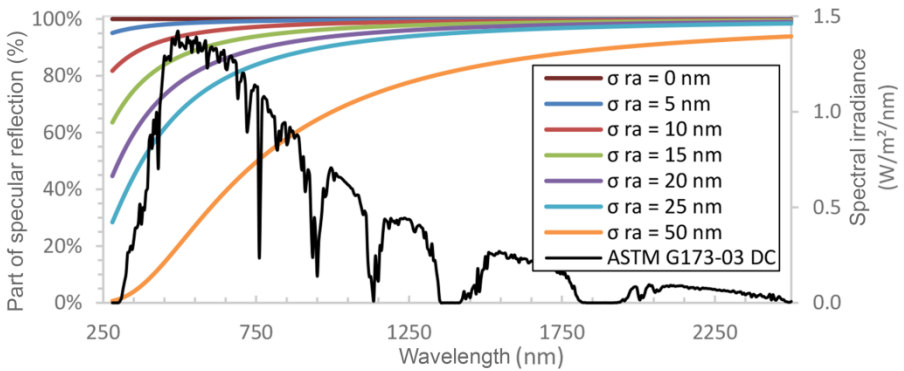


Figure 7.2. Part of the specular reflection in the total reflection as a function of the incident wavelength (normal incidence) for various roughness values σ_{ra}

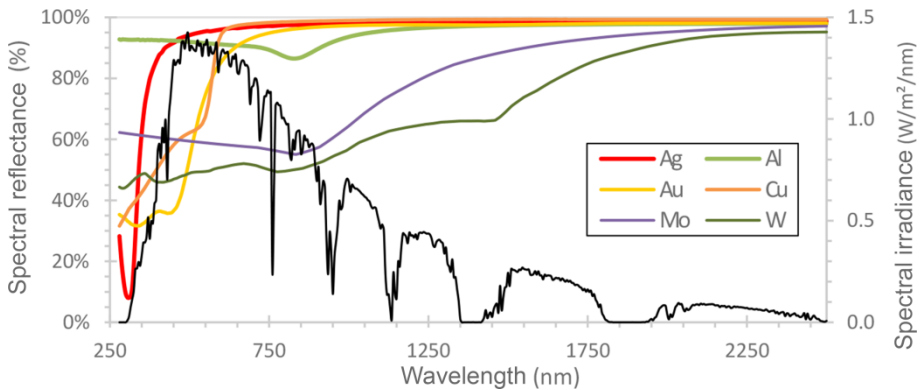


Figure 7.3. Theoretical spectral reflectance of pure metals in the solar range

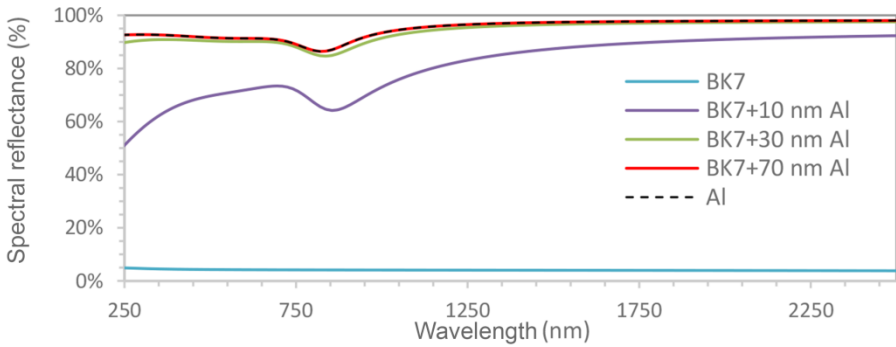


Figure 7.4. Simulated spectral reflectance of pure Al and Al thin films of various thicknesses deposited on a BK7 glass slide

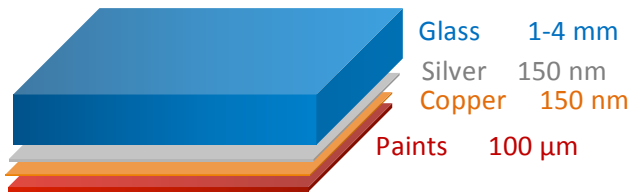


Figure 7.5. Architecture of a silver-based solar mirror

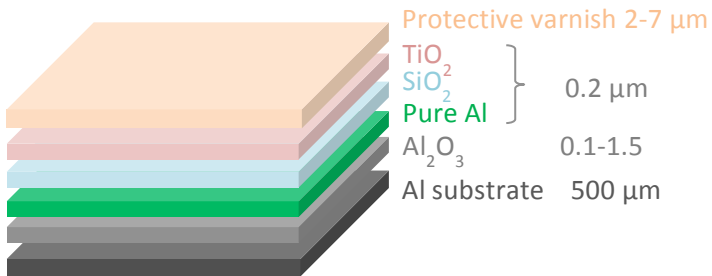


Figure 7.6. Architecture of an aluminum-based mirror

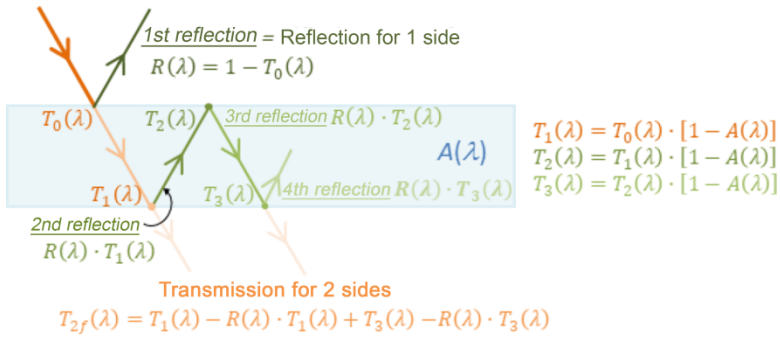


Figure 7.7. Reflection at the two interfaces of a glass and transmission for two sides

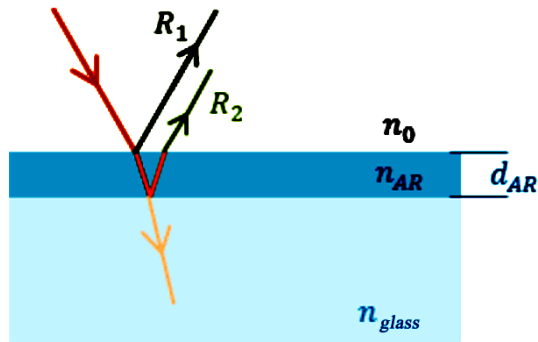


Figure 7.8. Reflection at the interfaces of a glass coated with antireflective layer (AR)

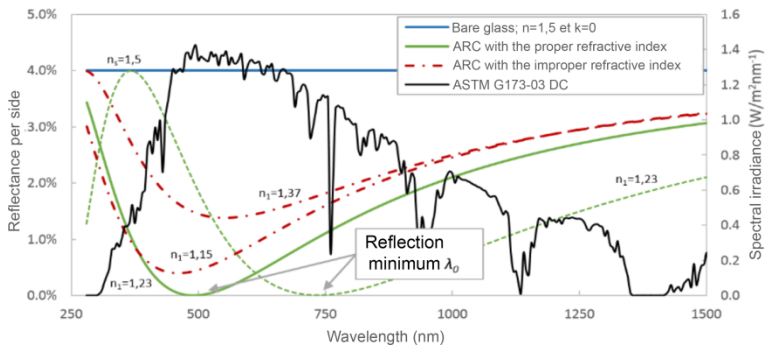


Figure 7.9. Reflection on a glass with ideal or non-ideal antireflective coating

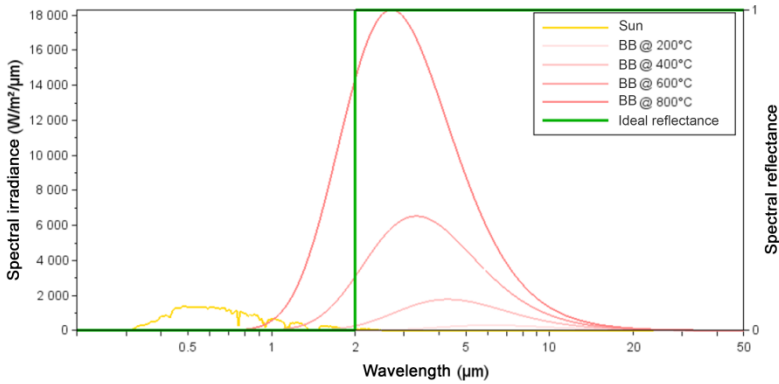


Figure 7.10. Spectral irradiances of Sun and black body (BB) at various temperatures; ideal spectral reflectance of a solar selective absorber

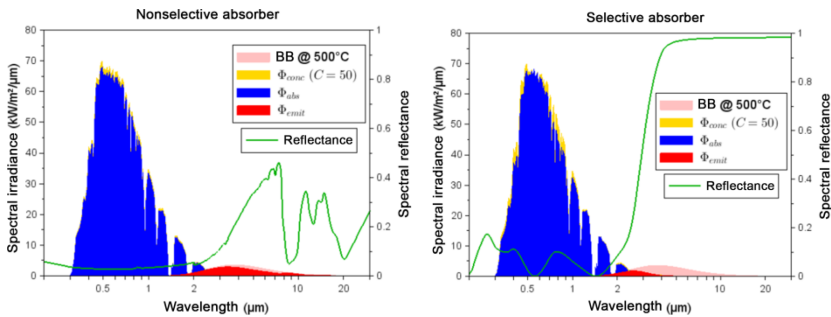


Figure 7.11. Spectral reflectance (green) and flux densities concentrated (yellow), absorbed (blue) and emitted at 500°C (red), for two types of absorbers

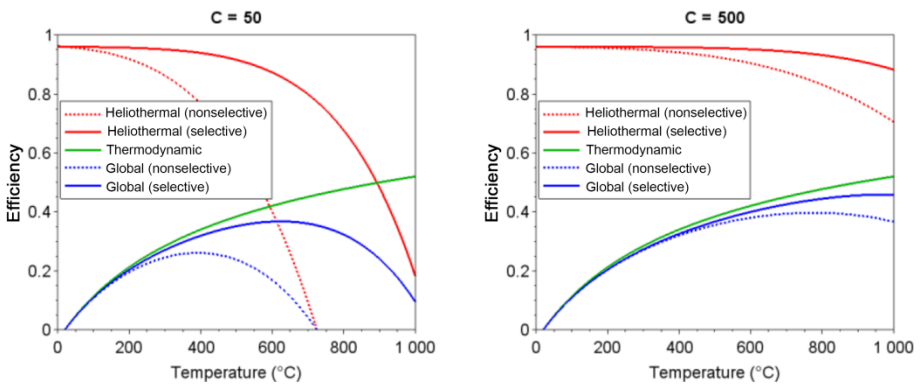


Figure 7.12. Efficiencies of solar-to-heat (heliothermal) conversion, heat-to-work (thermodynamic) conversion and solar-to-work (global) conversion depending on the operating temperature, for two concentration ratios C

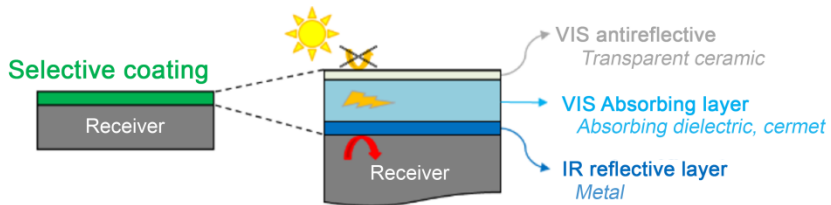


Figure 7.13. Architecture of a solar selective absorber coating

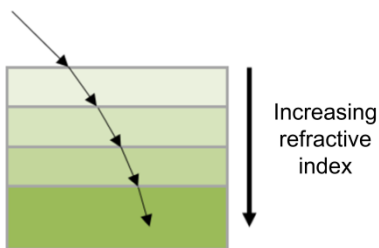


Figure 7.14. Accommodation of refractive indices and trapping of incident radiation

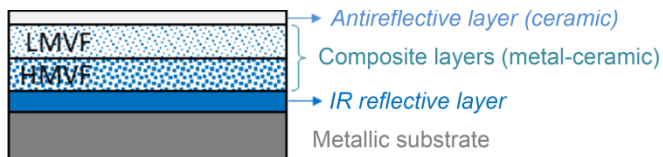


Figure 7.15. Classical architecture of a composite absorber

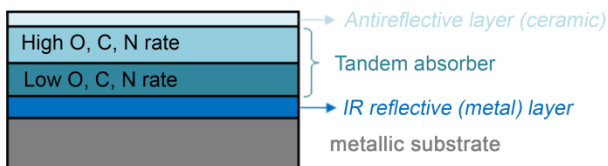


Figure 7.16. Classical architecture of a tandem absorber



Figure 8.2. Andasol power plant; the storage tanks are visible in the upper right

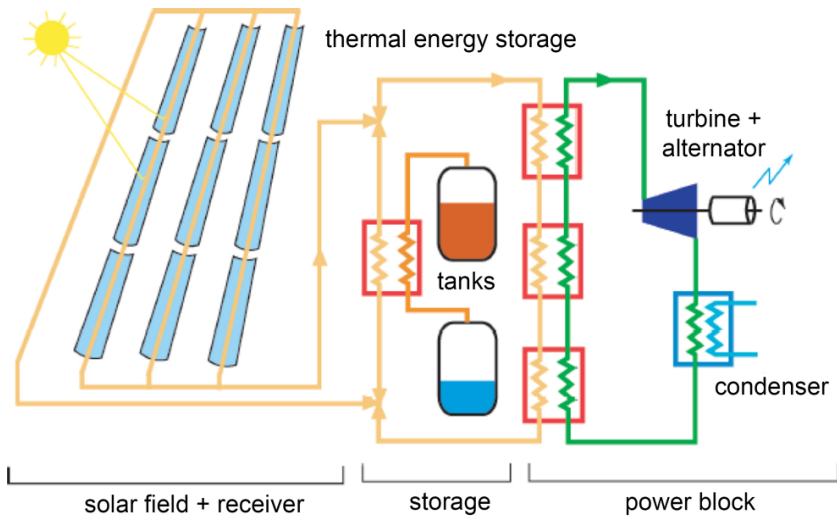


Figure 8.3. Simplified diagram of the components of Andasol power plant (Odrů et al. Forthcoming)

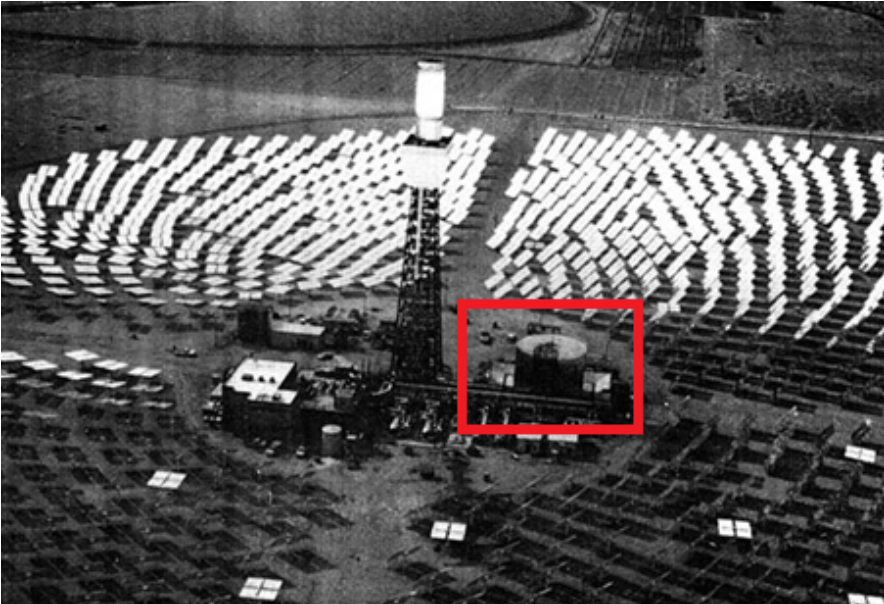


Figure 8.4. Solar One solar power plant (storage framed in red)

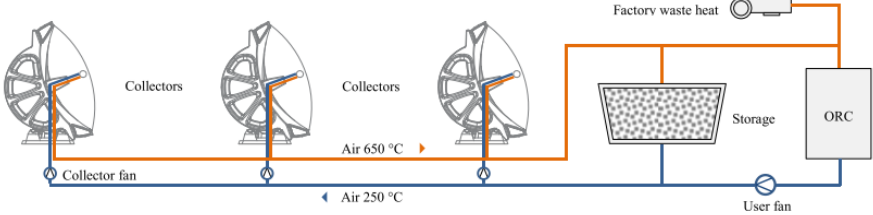


Figure 8.5. Process diagram of the power plant in Ait-Baha (Good et al. 2014)



Figure 8.6. Eco-Stock thermocline storage used to store 2 MWh heat on an industrial site (Eco-Tech Ceram)

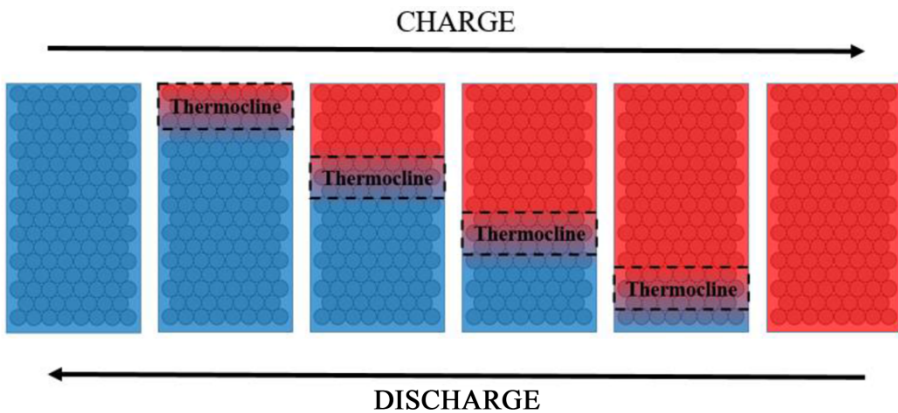


Figure 8.7. Diagram of thermocline development

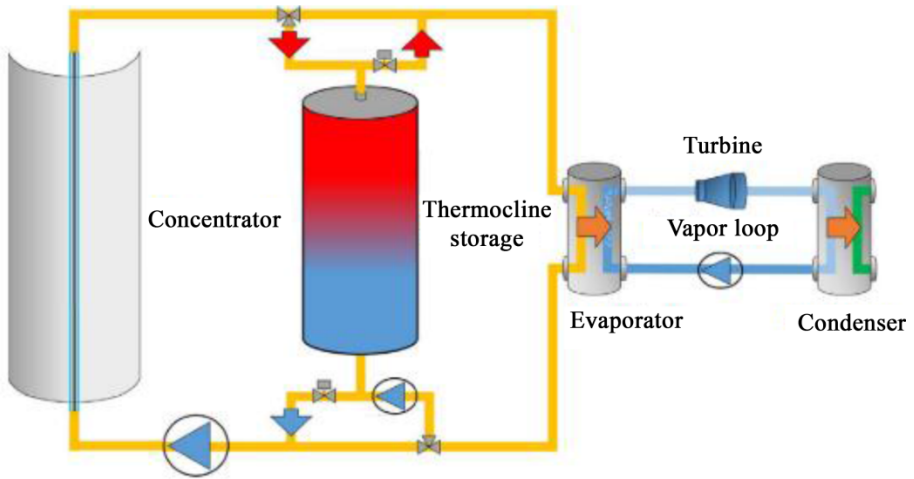


Figure 8.8. Storage integration in a solar power plant, adapted from Fasquelle et al. (2018)

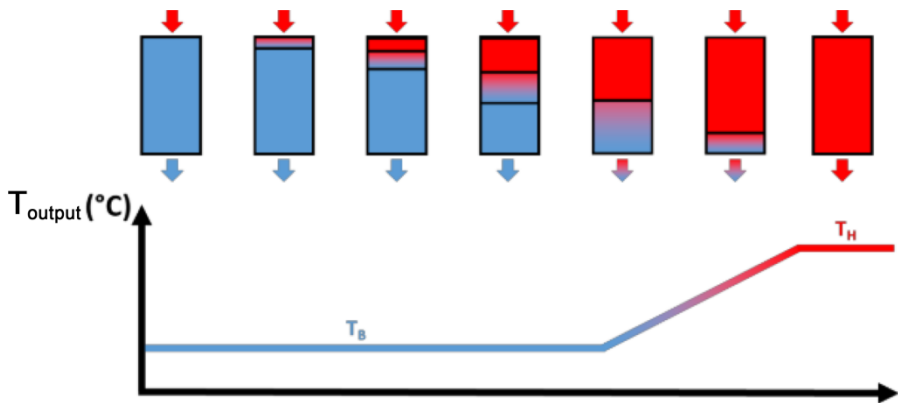


Figure 8.9. Extraction of thermocline during charging (Fasquelle 2017)

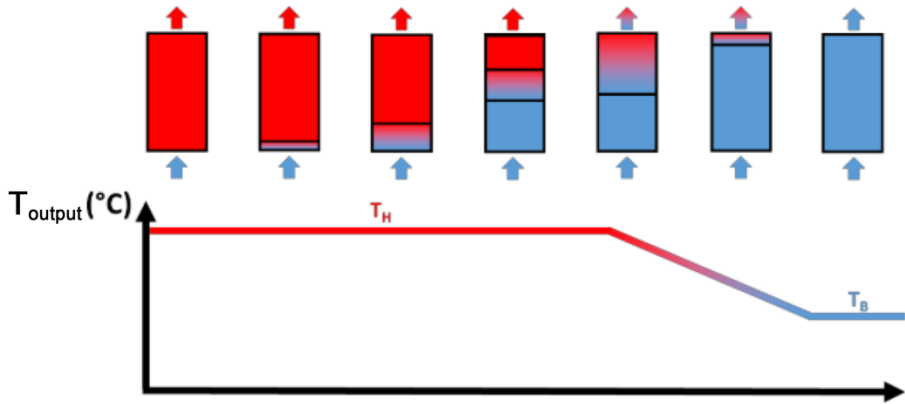


Figure 8.10. Thermocline extraction during discharge (Fasquelle 2017)



Figure 8.11. Examples of structured materials

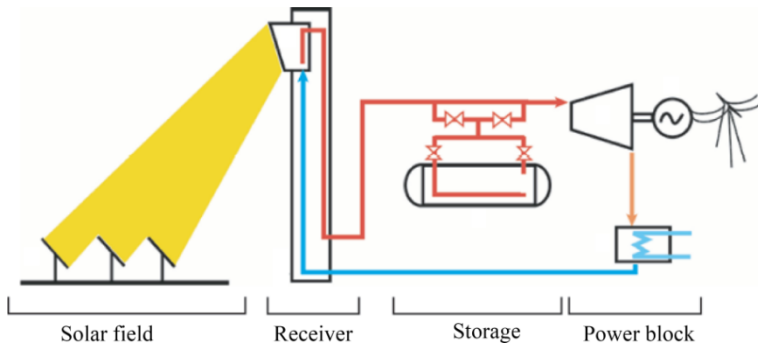


Figure 8.12. Diagram of a solar power plant with direct steam generation (Odrů et al. Forthcoming)



Figure 8.13. *Four steam accumulators of the PS10 power plant (Abengoa Solar)*



Figure 8.14. *Image of the storage tanks of eLLO power plant (SUNCNIM)*

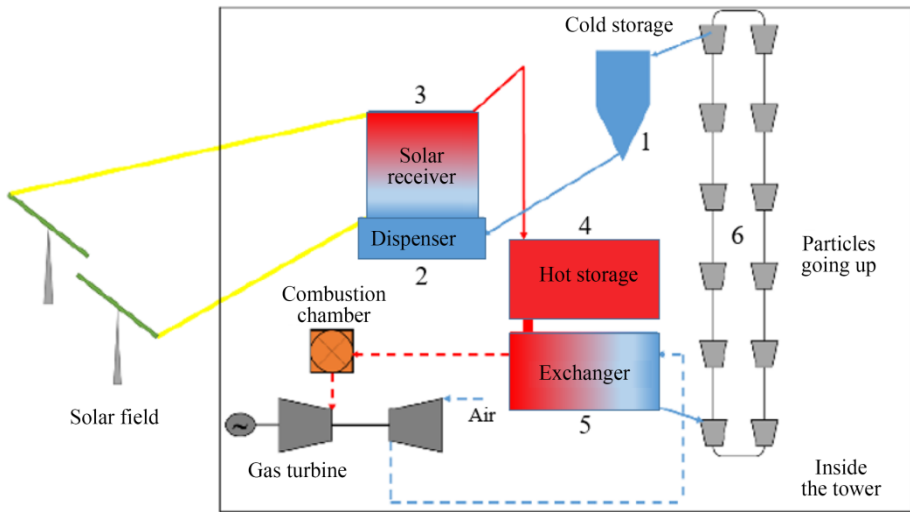


Figure 8.16. Diagram of a solar power plant with fluidized bed (adapted from Grange et al. 2020)



Figure 8.17. Pilot PCM storage by CEA-Liten (Garcia et al. 2015)

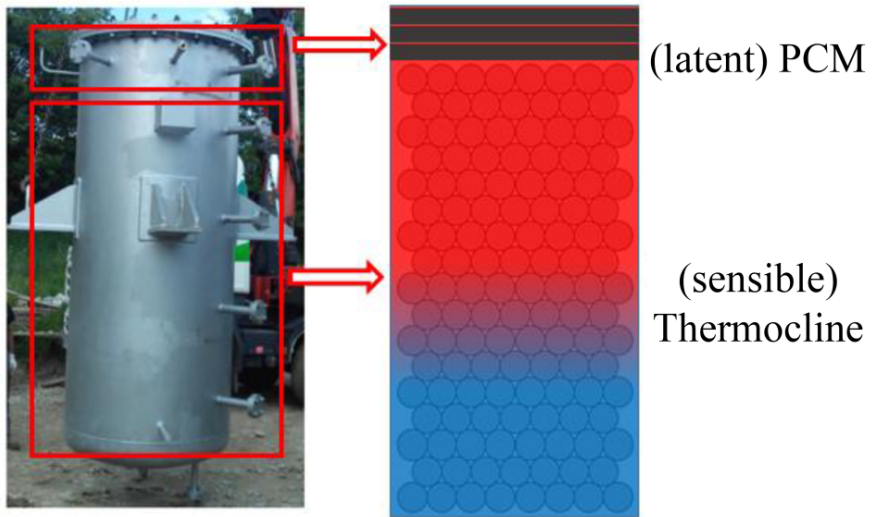


Figure 8.18. Integration of an encapsulated PCM in a thermocline storage

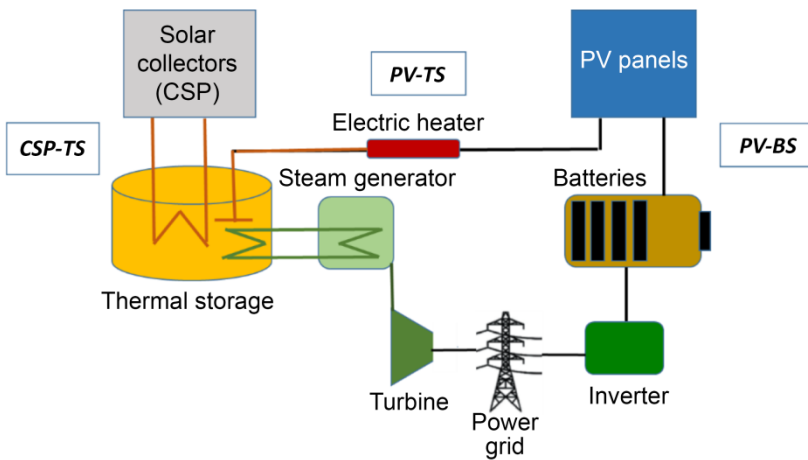


Figure 8.20. Diagram of the three architectures for solar energy storage compared by Schöniger et al. (2020)

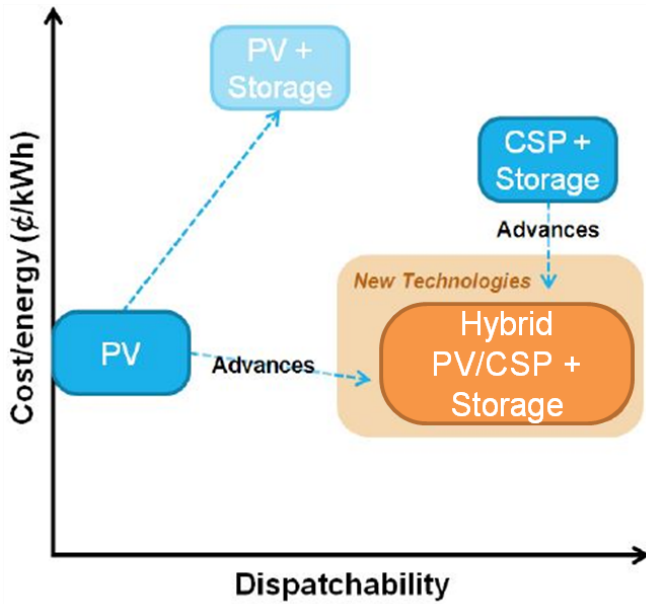


Figure 9.1. Cost and dispatchability comparison between PV technologies (with and without storage), CSP systems and hybrid PV/CSP systems (source: FOCUS n.d.)

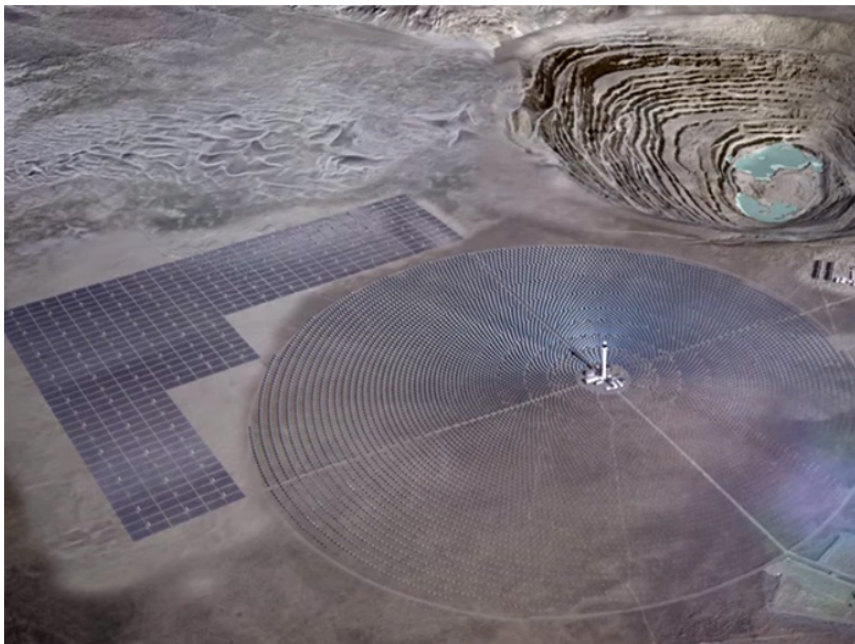


Figure 9.3. An artist's view of the non-compact hybrid PV–CSP power plant of Copiapó (Chile) (source: IEEE Spectrum n.d.)

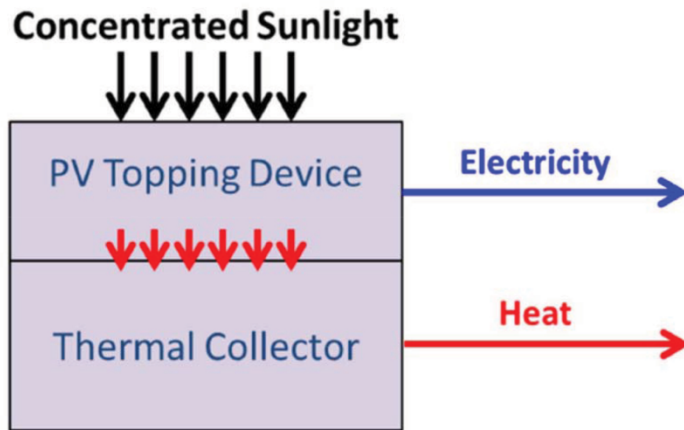


Figure 9.4. Schematic representation of a “high-temperature” integrated PV–CSP receiver. The concentrated solar radiation is absorbed by a high-temperature PV module that is also a thermal collector. Part of the incident solar energy is directly converted into electricity while the rest is transferred in the form of heat to the thermal collector (Branz et al. 2015)

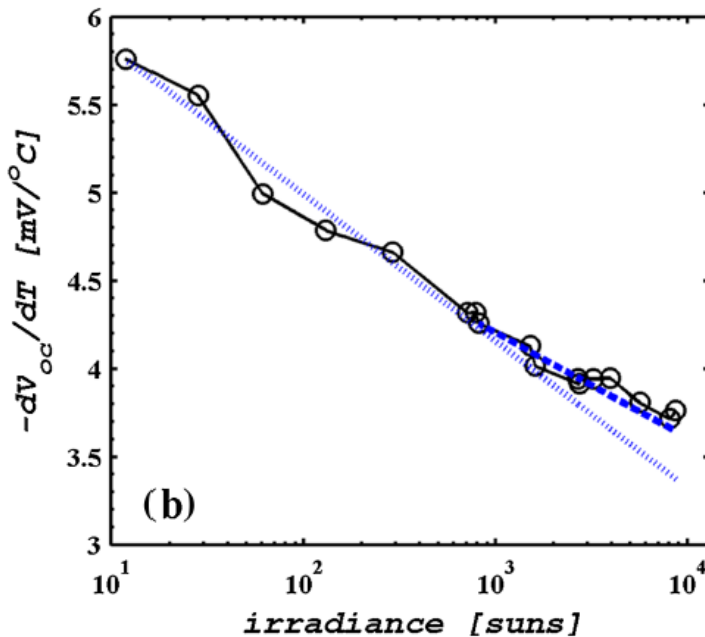


Figure 9.6. Temperature coefficient of V_{oc} as a function of the solar concentration ratio, for a InGaP/InGaAs/Ge multi-junction solar cell (Braun et al. 2013)

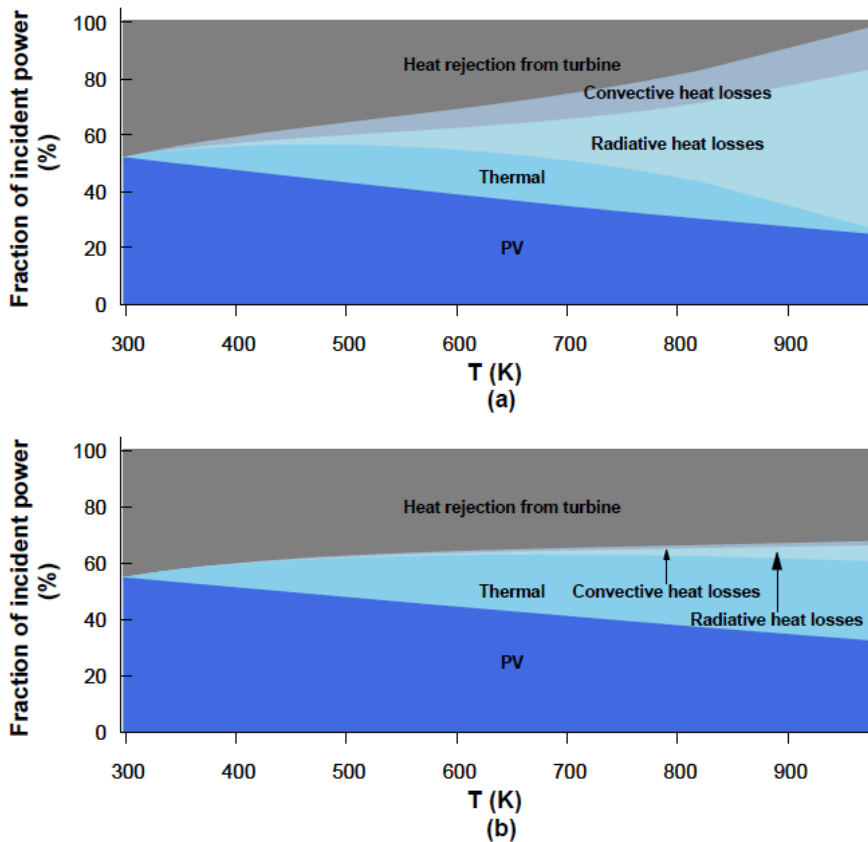


Figure 9.7. PV, thermal and hybrid conversion efficiencies as a function of the operating temperature and the associated heat losses for cells operating at the radiative limit under a concentration of 100 suns (a) and at the radiative limit under 1,000 suns (b) (Zeitouny et al. 2018)

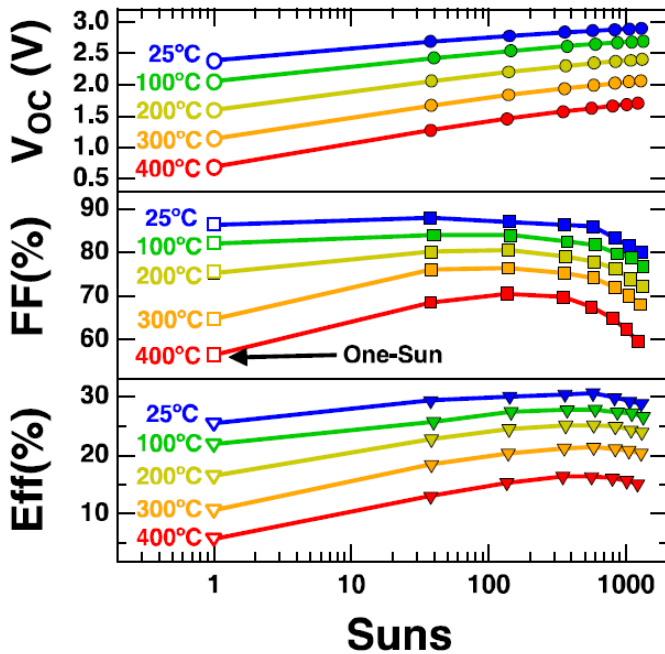


Figure 9.8. Open circuit voltage (V_{oc}), fill factor (FF) and conversion efficiency of a GaInP/GaInAs tandem cell as a function of solar concentration and for temperatures ranging between 25°C and 400°C (Perl et al. 2018)

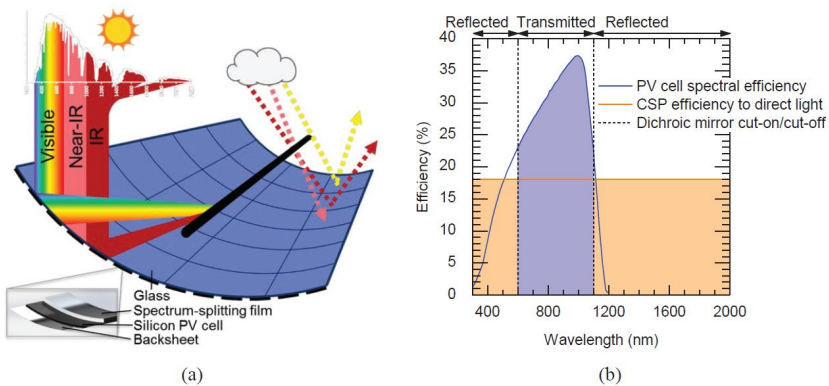


Figure 9.9. Schematic representation of the hybrid “PV-mirror” system developed at Arizona State University (a) and diagram representing spectral efficiencies of PV cells and CSP converter, and the ranges of wavelengths used by each converter (Fisher et al. 2017)

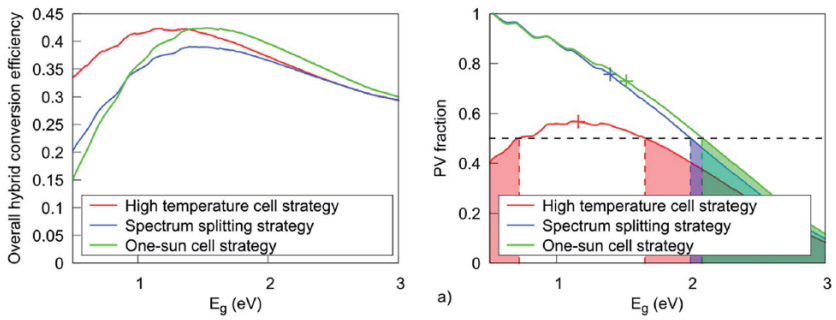


Figure 9.11. Global conversion efficiency (left) and PV fraction (right) for three compact hybrid strategies, as a function of the energy band gap of the PV cell, and for PV cells operating at the radiative limit (Vossier et al. 2018)

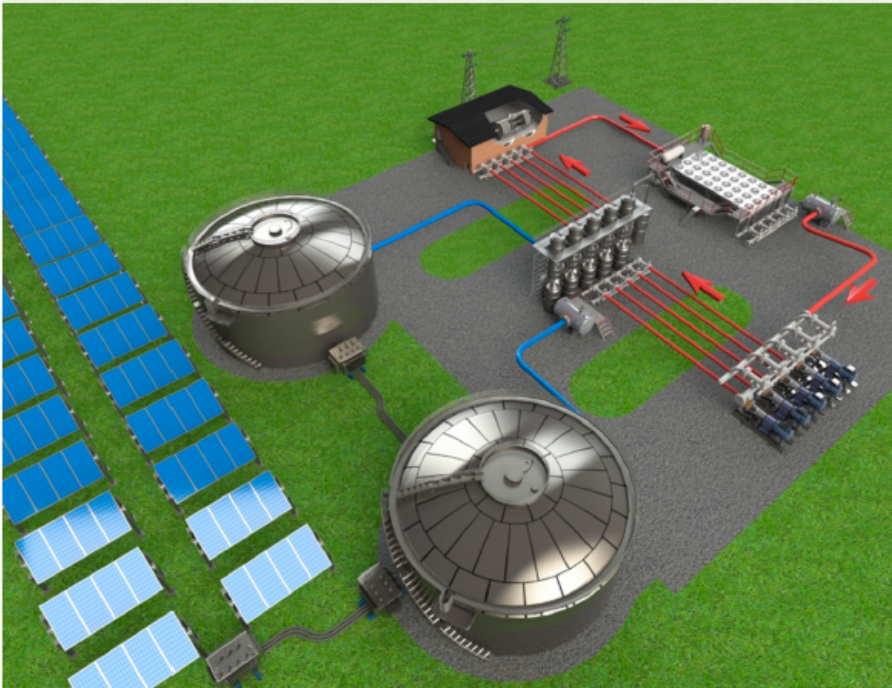


Figure 9.12. Illustration of the PV + thermal storage + steam turbine concept (Gordon et al. 2021)

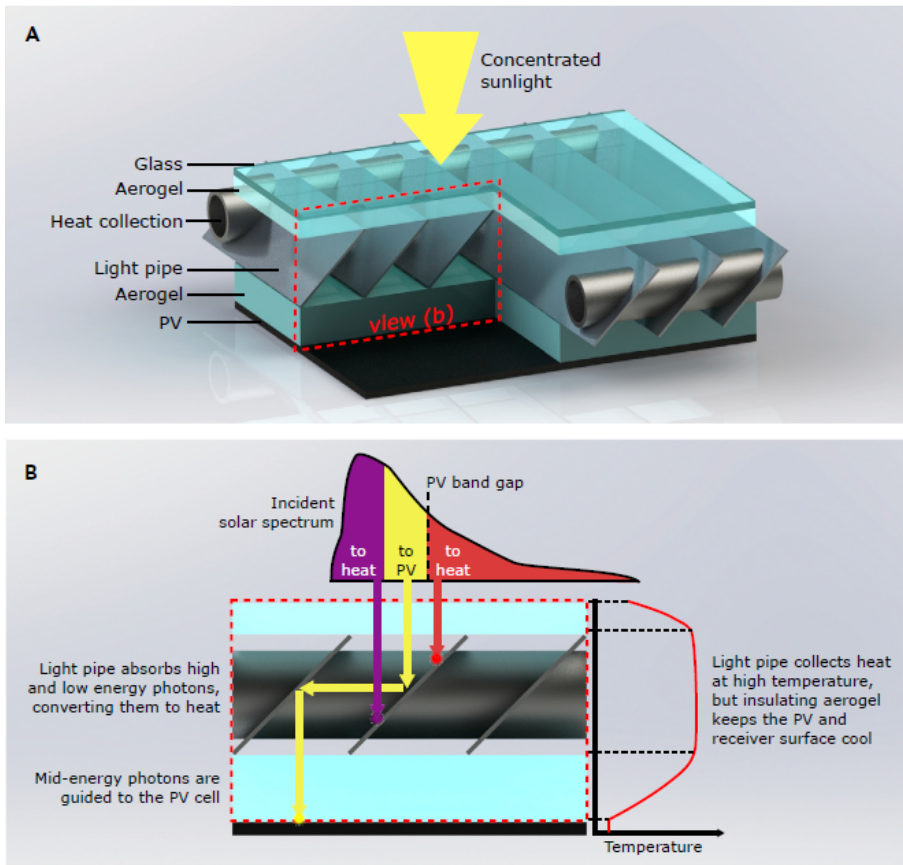


Figure 9.13. Schematic representation of the HEATS concept. The module consists of a stack of several elements, notably a glass protection, an aerogel layer acting as thermal insulator, spectrally selective light pipes, another aerogel layer and, finally, PV cells. The light pipes contain parallel fins that are coated with a selective coating. These fins are attached to the light pipes, to which they transmit the harvested heat. The latter is absorbed by the heat transfer fluid and is then carried to the thermal storage system (Weinstein et al. 2018)

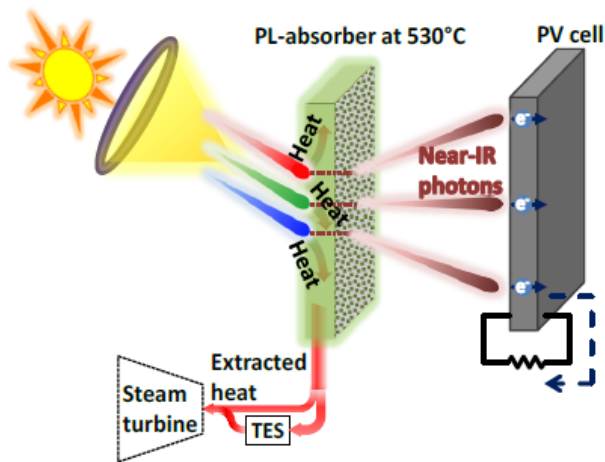


Figure 9.14. Illustration of LSC concept. (a) The solar flux is concentrated on photo-luminescent absorber. The radiation emitted by photo-luminescence (whose spectrum is red shifted) is absorbed by a solar cell whose energy band gap is adapted, while the residual heat (at 530°C) is stored to be injected in a turbine (Haviv et al. 2020)

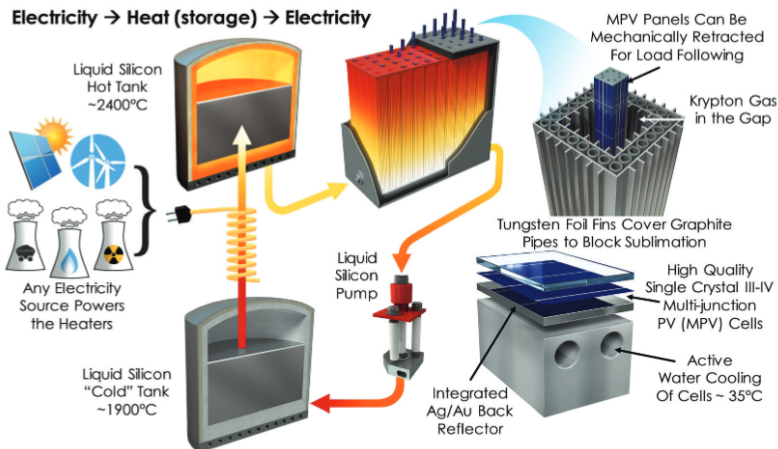


Figure 9.15. Schematic representation of TEGS-MPV concept: electricity is converted in the form of heat through a heating resistor, before being transferred to a liquid storage in the form of latent heat (1,900–2,400°C). Low-cost metallurgical-grade silicon is used as storage material. When electricity must be generated, the liquid is pumped through a set of pipes, emitting radiation converted into electricity by multi-junction cells located at the center of the set (Amy et al. 2019)

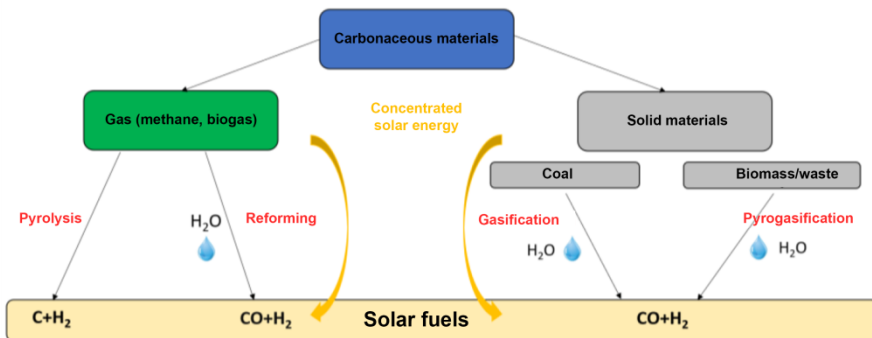


Figure 10.1. Main processes for manufacturing synthetic fuels from hydrocarbon resources

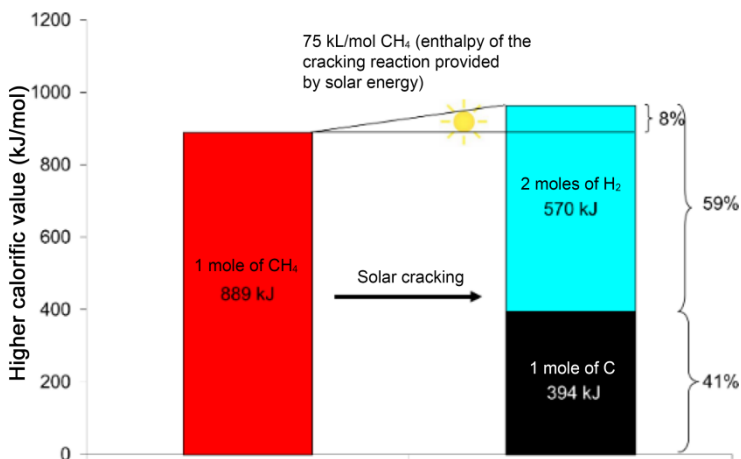


Figure 10.3. Energy balance of the solar cracking of methane (adapted from Rodat et al. 2010)

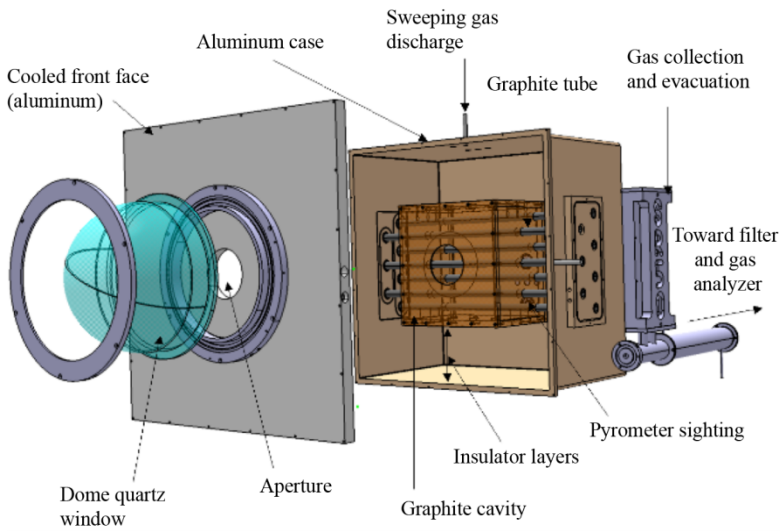


Figure 10.5. Indirect heating solar reactor for methane cracking

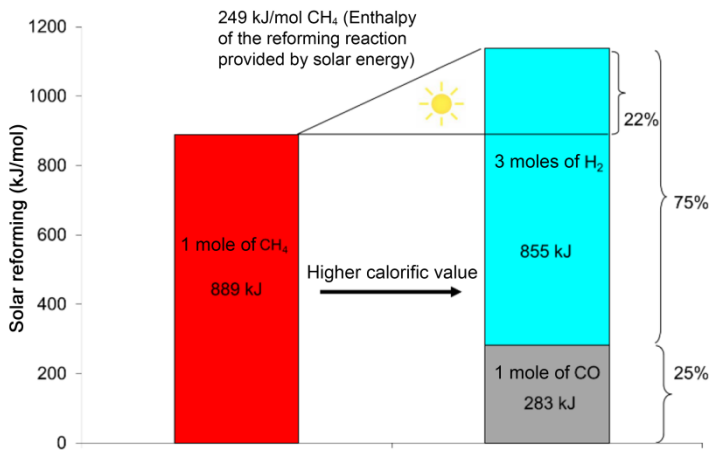


Figure 10.7. Energy balance of the solar steam reforming of methane

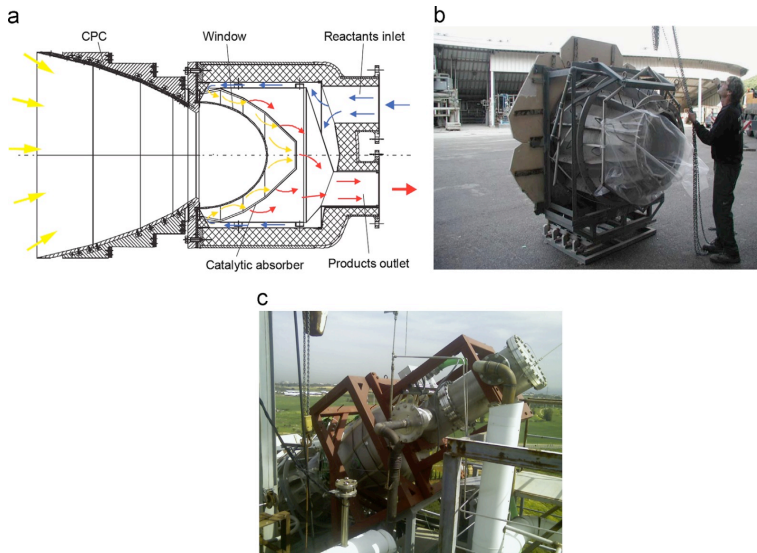


Figure 10.9. Solar reformer with direct heating: (a) schematic diagram, (b) assembled reactor, (c) reactor installed on top of the solar tower at Weizmann Institute of Science in Israel (Agrafiotis et al. 2014)

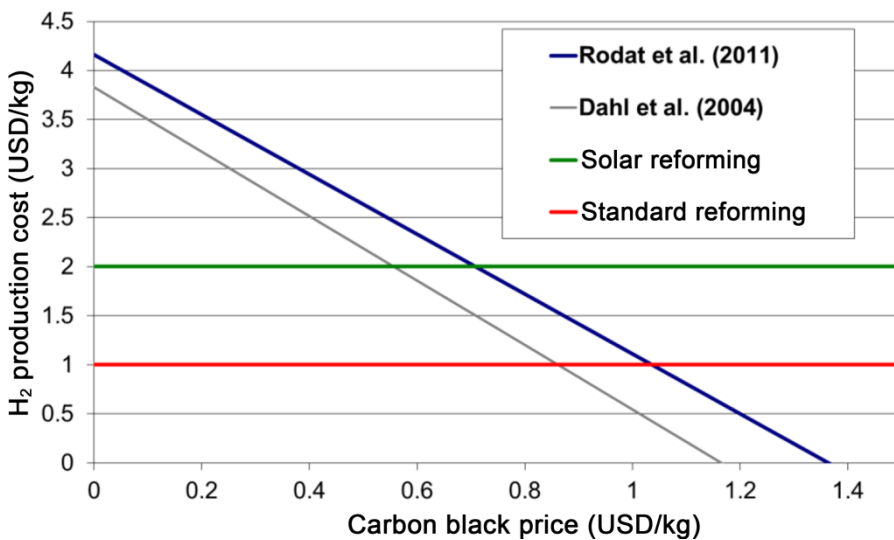


Figure 10.10. Hydrogen production cost depending on the carbon black price compared to solar reforming and conventional reforming (Rodat et al. 2011)

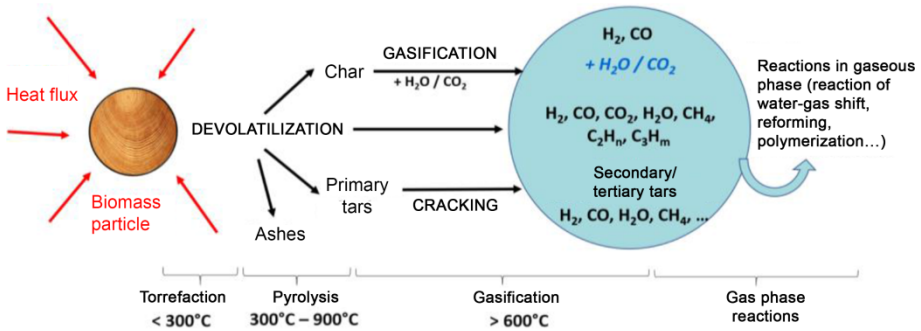


Figure 10.11. Thermochemical conversion of biomass

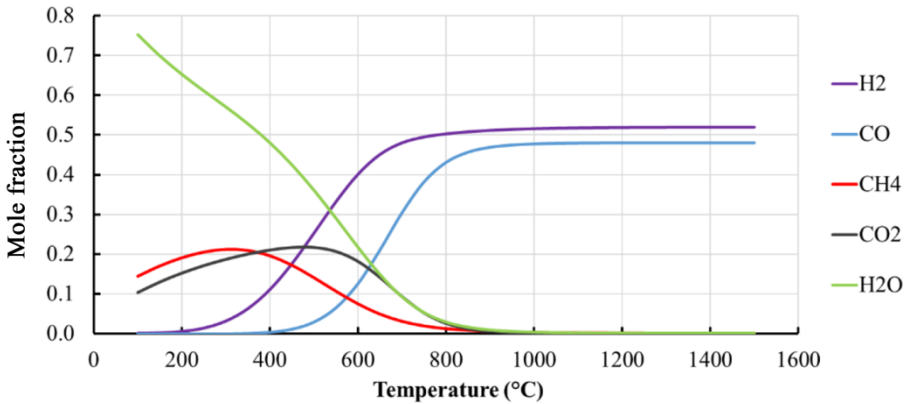


Figure 10.12. Evolution of the composition at thermodynamic equilibrium of synthetic gas during wood gasification with water depending on the temperature ($C_6H_5O_4 + 2H_2O$) (adapted from Bellouard et al. 2020)

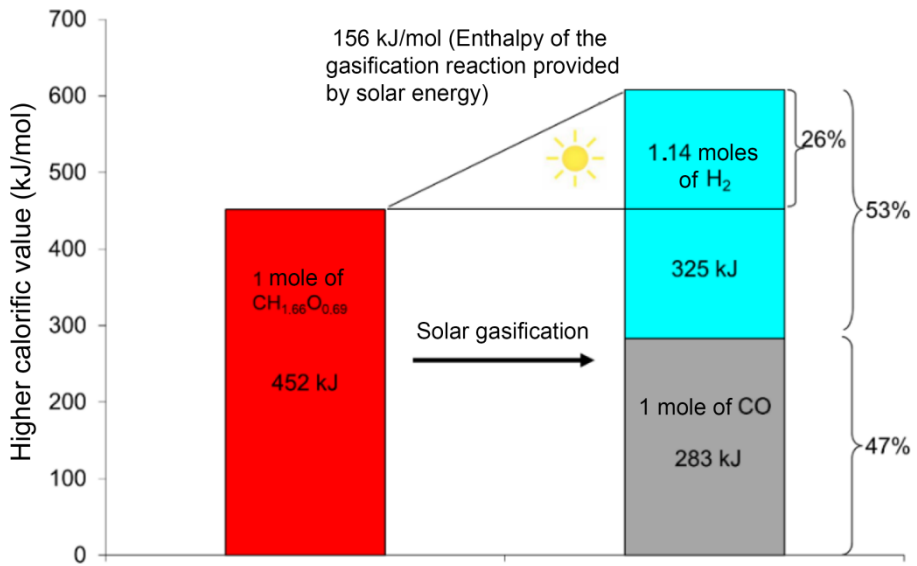


Figure 10.13. Energy balance of solar gasification of biomass (beech wood, formula $CH_{1.66}O_{0.69}$)

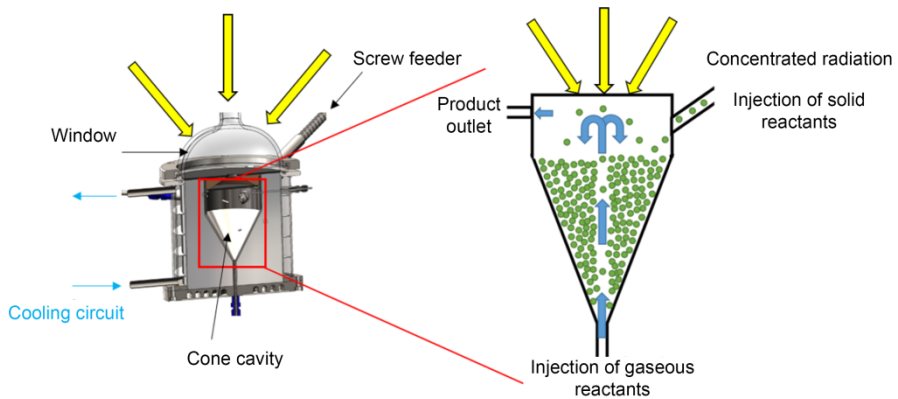


Figure 10.15. 3D view and schematic representation of the spouted bed reactor (1.5 kW)

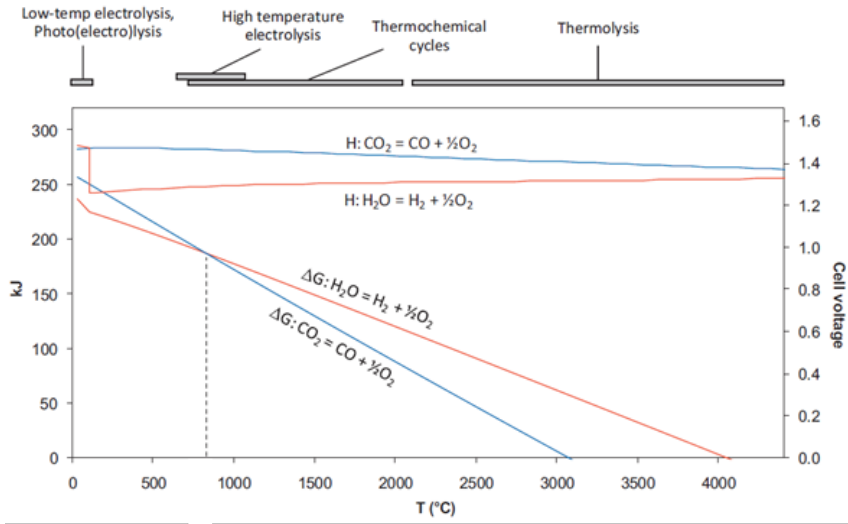


Figure 11.1. Evolution of enthalpy and free energy associated with CO₂ and H₂O thermolysis as a function of temperature

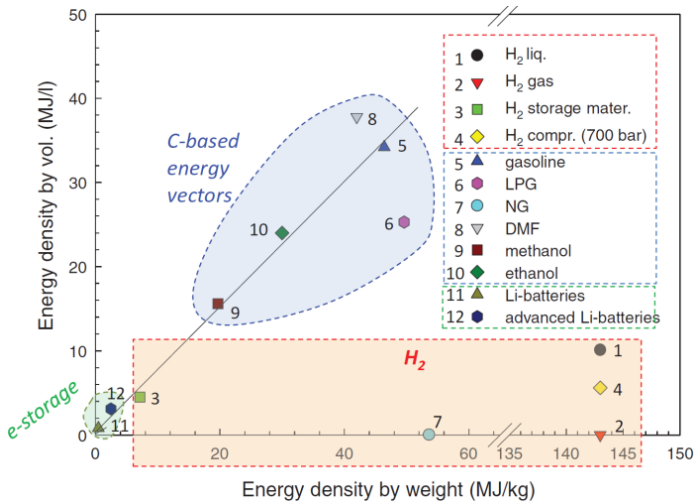


Figure 11.2. Comparison of energy densities by weight and by volume for various energy vectors (Centi and Perathoner 2011)

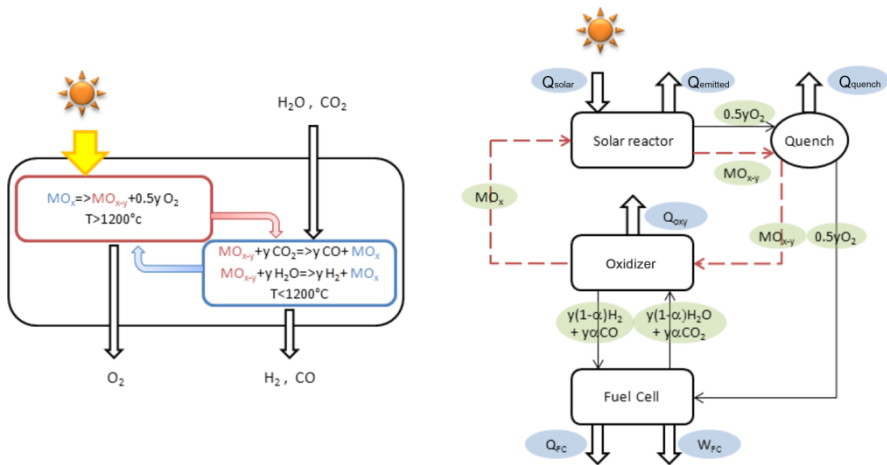


Figure 11.3. Mass and energy diagram for a thermochemical cycle

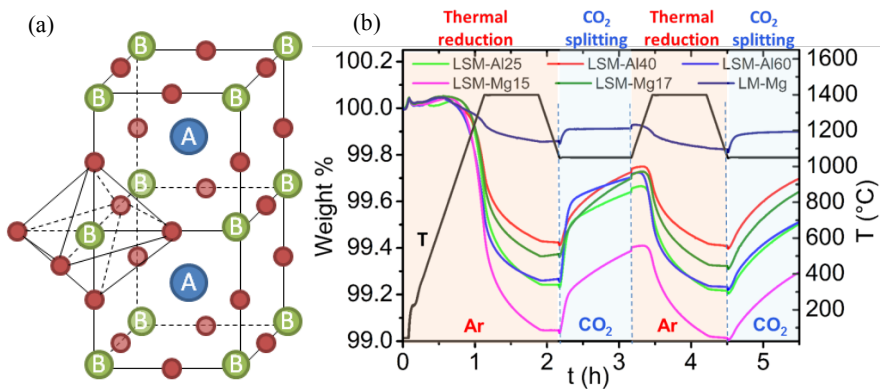


Figure 11.4. (a) ABO_3 perovskite structure; (b) reactivity of LSM perovskites doped with Al or Mg at B site during two successive cycles (reduction under Ar at 1,400°C and oxidation under CO_2 at 1,050°C)

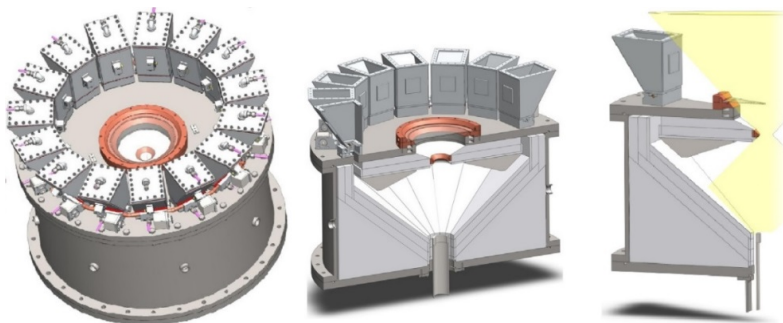


Figure 11.9. Diagram of the reactor with gravity-driven injection of particles

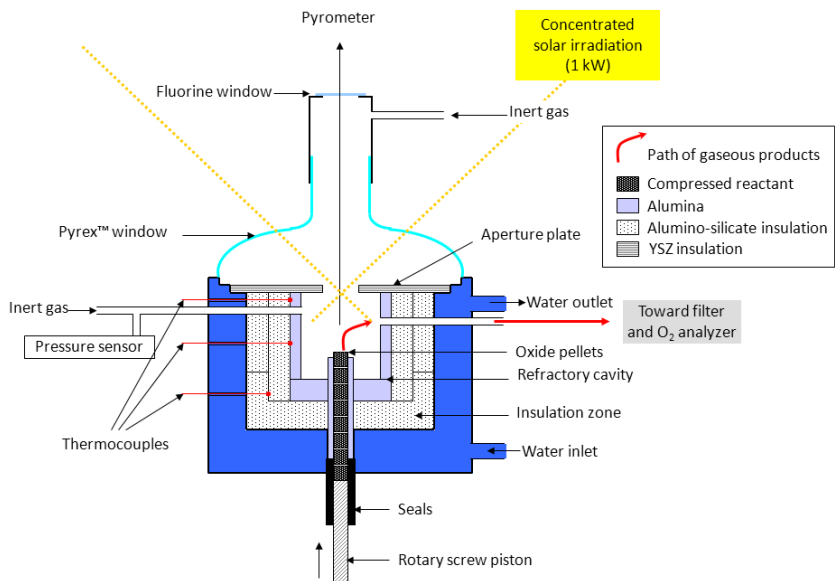


Figure 11.10. Reactor for the dissociation of volatile oxides (ZnO , SnO_2) with continuous injection of reactant in compressed form

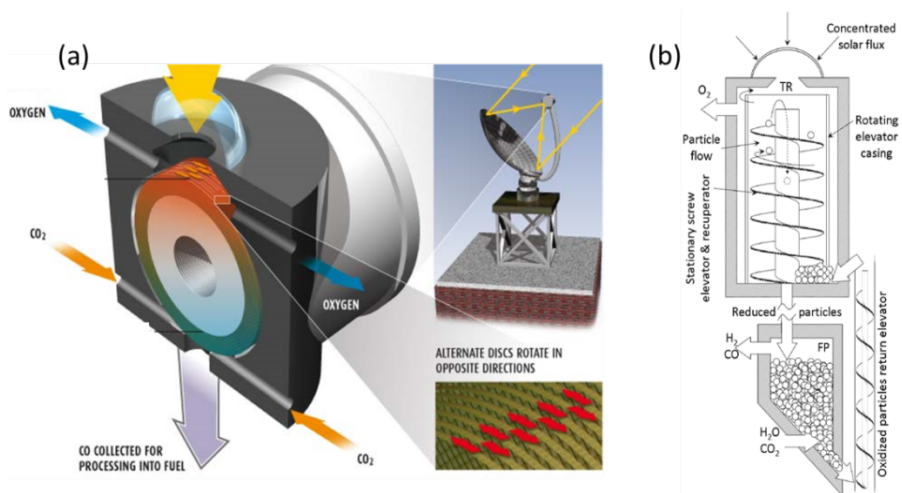


Figure 11.11. (a) Diagram of CR5 reactor and (b) prototype of circulating dense bed reactor